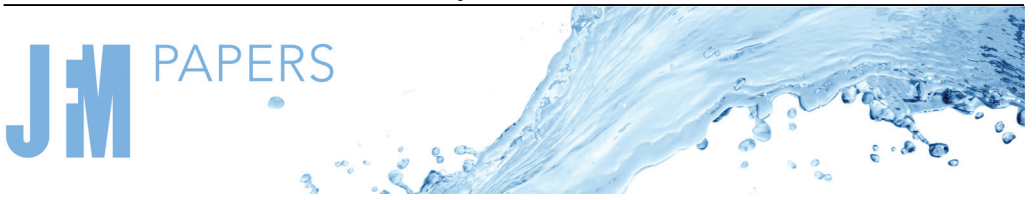
J. Fluid Mech. (2024), *vol*. 996, A33, doi:10.1017/jfm.2024.674



Magneto-Stokes flow in a shallow free-surface annulus

Cy S. David[1,†], **Eric W. Hester**[2], **Yufan Xu**[1,3] **and Jonathan M. Aurnou**[1]

[1]Department of Earth, Planetary, and Space Sciences, University of California, Los Angeles, CA 90095, USA

[2]Department of Mathematics, University of California, Los Angeles, CA 90095, USA

[3]Princeton Plasma Physics Laboratory, Princeton, NJ 08540, USA

(Received 27 October 2023; revised 8 May 2024; accepted 19 June 2024)

In this study, we analyse 'magneto-Stokes' flow, a fundamental magnetohydrodynamic (MHD) flow that shares the cylindrical-annular geometry of the Taylor–Couette cell but uses applied electromagnetic forces to circulate a free-surface layer of electrolyte at low Reynolds numbers. The first complete, analytical solution for time-dependent magneto-Stokes flow is presented and validated with coupled laboratory and numerical experiments. Three regimes are distinguished (shallow-layer, transitional and deep-layer flow regimes), and their influence on the efficiency of microscale mixing is clarified. The solution in the shallow-layer limit belongs to a newly identified class of MHD potential flows, and thus induces mixing without the aid of axial vorticity. We show that these shallow-layer magneto-Stokes flows can still augment mixing in distinct Taylor dispersion and advection-dominated mixing regimes. The existence of enhanced mixing across all three distinguished flow regimes is predicted by asymptotic scaling laws and supported by three-dimensional numerical simulations. Mixing enhancement is initiated with the least electromagnetic forcing in channels with order-unity depth-to-gap-width ratios. If the strength of the electromagnetic forcing is not a constraint, then shallow-layer flows can still yield the shortest mixing times in the advection-dominated limit. Our robust description of momentum evolution and mixing of passive tracers makes the annular magneto-Stokes system fit for use as an MHD reference flow.

Key words: mixing enhancement

1. Introduction

The year 2023 marked the 100th anniversary of G.I. Taylor's seminal publication (Taylor 1923) on flow confined between two rotating concentric cylinders (Taylor–Couette flow)

† Email address for correspondence: cysdavid@ucla.edu

© The Author(s), 2024. Published by Cambridge University Press. This is an Open Access article, distributed under the terms of the Creative Commons Attribution-NonCommercial-ShareAlike licence (http://creativecommons.org/licenses/by-nc-sa/4.0), which permits non-commercial re-use, distribution, and reproduction in any medium, provided the same Creative Commons licence is used to distribute the re-used or adapted article and the original article is properly cited. The written permission of Cambridge University Press must be obtained prior to any commercial use.

https://doi.org/10.1017/jfm.2024.674 Published online by Cambridge University Press

and the 70th anniversary of his work (Taylor 1953) on enhanced mixing in shear flows (Taylor dispersion). With these two landmark papers in mind, we develop a magnetohydrodynamic (MHD) reference flow inspired by the Taylor–Couette system that enhances mixing at low Reynolds numbers via Taylor dispersion.

Our MHD modification of the Taylor–Couette cell uses electromagnetic body forces rather than viscous traction to drive motion; the usually rotating sidewalls of the cylindrical annulus are fixed and made electrically conducting. The base is kept electrically insulating, while the lid is removed to allow free-surface flow. An applied axial magnetic field and radial electric current drive azimuthal flow of an electrolyte, for which (i) magnetic induction is small compared with magnetic diffusion (low magnetic Reynolds number, Rm), (ii) magnetic drag is small relative to viscous forces (low Hartmann number, Ha), and (iii) inertia is small compared with viscous forces (low Reynolds number, Re). Under these conditions, the azimuthal momentum balance is dominated by the Lorentz force and viscous drag due to the channel sidewalls and base. We term the resulting circulatory motion 'annular magneto-Stokes flow'.

Similar MHD flows through cylindrical-annular ducts with conducting sidewalls and axial magnetic field have been considered since the works of Early & Dow (1950), Anderson *et al.* (1959) and Braginsky (1959). Early modelling efforts focus on the high-Hartmann-number limit for analytical convenience (Hunt & Stewartson 1965) and relevance to liquid metal flows (Baylis & Hunt 1971). Later numerical and laboratory works have surveyed a broader range of Hartmann numbers in closed annular ducts (Poyé *et al.* 2020; Vernet *et al.* 2021), analysed the stability of Hartmann layers (Moresco & Alboussire 2004) and studied the effects of modified electric boundary conditions (Stelzer *et al.* 2015*a*,*b*) in cylindrical-annular MHD flows. Recently, liquid metal experiments (Vernet, Fauve & Gissinger 2022) in a similar geometry have accessed a regime of Keplerian turbulence representative of flows in astrophysical disks.

In contrast to the above studies involving large-scale liquid metal systems, applications of MHD to microfluidic mixing devices have generated interest in low-Hartmann-number flows (West *et al.* 2003; Khal'zov & Smolyakov 2006) appropriate for electrolytes. Initial efforts to model annular magneto-Stokes flow (Gleeson & West 2002; Gleeson *et al.* 2004; Digilov 2007) assumed an infinitely deep layer, arriving at a two-dimensional (2-D) asymptotic solution. Pérez-Barrera *et al.* (2015) and Pérez-Barrera, Ortiz & Cuevas (2016) later considered channels of finite depth, solving specifically for the vertically averaged velocity profile $\langle u_\theta \rangle_z(r)$. Following this, Ortiz-Pérez *et al.* (2017) and Valenzuela-Delgado *et al.* (2018*a*,*b*) used a (semi-analytical) Galerkin approximation to predict steady, axisymmetric flow over radius and depth, $u_\theta(r, z)$. A fully analytical solution $u_\theta(r, z, t)$ for time-dependent annular magneto-Stokes flow does not exist in the literature, to our knowledge, despite the simplicity of the governing equation. Further, there is little discussion of the range of channel geometries for which the deep-layer approximation is valid. Yet, the assumption of infinite depth has been made for engineering problems involving shallow-layer flows (e.g. West *et al.* 2003) with strong vertical shear that depart greatly from the 2-D deep-layer solution.

In this study, we unify and extend these previous efforts by: (i) providing the first complete analytical solution for time-dependent flow $u_\theta(r, z, t)$ in a channel of arbitrary depth (§ 2), which we validate with laboratory experiments and direct numerical simulations (DNS) (§§ 3, 4); (ii) correctly distinguishing deep, transitional and shallow-layer flow regimes in terms of the appropriate geometric parameter (§ 2); (iii) deriving the shallow-layer asymptotic solution (§ 2); (iv) applying these findings to the design of a microfluidic mixer (§ 5); and (v) showing that the onset of shear-enhanced mixing occurs with the least electromagnetic forcing in the transitional flow regime (§ 5).

https://doi.org/10.1017/jfm.2024.674 Published online by Cambridge University Press

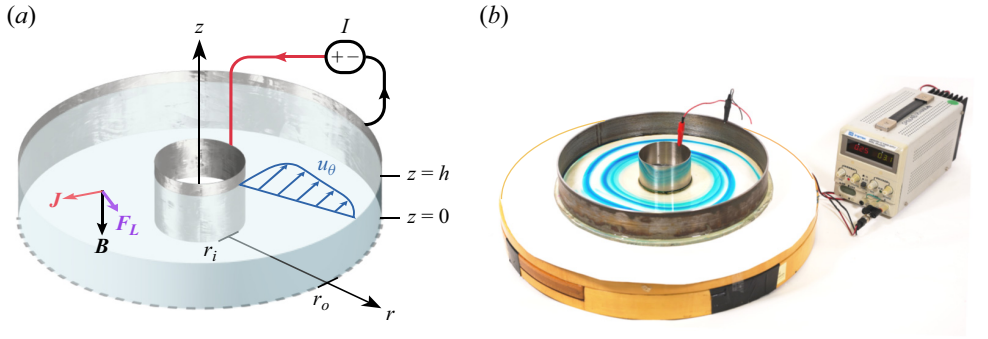


Figure 1. (*a*) Diagram of the magneto-Stokes system. A power supply controls the electric current I through the fluid layer. Radially outwards ($+\boldsymbol{e}_r$) current density $\boldsymbol{J}$ and downwards ($-\boldsymbol{e}_z$) magnetic field $\boldsymbol{B}$ produce an azimuthal ($+\boldsymbol{e}_\theta$) Lorentz force $\boldsymbol{F}$ on the fluid. (*b*) Photograph of the channel used in laboratory experiments, with flow visualised by blue dye. The channel rests atop a wooden case of permanent magnets, which is replaced by a solenoid electromagnet (not pictured) for cases I–IV discussed in § 3.

2. Theory

2.1. *Axisymmetric governing equations*

We consider a free-surface layer of conducting fluid of depth h in the annular gap between two cylindrical electrodes of radius r_i and r_o ($r_i < r_o$). A controlled current I runs through the fluid from inner to outer electrode, and the entire annulus is subject to a vertical, imposed magnetic field $\boldsymbol{B} = -B_0\boldsymbol{e}_z$. Figure 1(*a*) shows a schematic of the annular channel with the imposed magnetic field and current. For a low-conductivity fluid like saltwater and small B_0, the magnetic field is quasi-static (e.g. Knaepen & Moreau 2008; Favier *et al.* 2011; Davidson 2016; Verma 2017) and the total Lorentz force on the fluid may be expressed as the sum of the applied driving force and magnetic drag,

$$\boldsymbol{F} = \boldsymbol{J} \times \boldsymbol{B} = \sigma(\boldsymbol{E} \times \boldsymbol{B}) - \sigma B_0^2(u_r\boldsymbol{e}_r + u_\theta\boldsymbol{e}_\theta), \tag{2.1}$$

after using Ohm's law to express the current density $\boldsymbol{J}$ in terms of the electrical conductivity of the fluid σ, the imposed electric field $\boldsymbol{E}$ and the fluid velocity $\boldsymbol{u}$.

Letting U denote a characteristic velocity scale, the magnitude of the magnetic drag ($\sim\sigma B_0^2 U$) may be compared with that of the viscous drag ($\sim\varrho\nu U/h^2$) by means of the Hartmann number,

$$Ha = \sqrt{\frac{\sigma B_0^2 U}{\varrho\nu U/h^2}} = B_0 h\sqrt{\frac{\sigma}{\varrho\nu}}, \tag{2.2}$$

where ϱ and ν are the density and kinematic viscosity of the fluid, respectively.

In our experiments, $Ha \lesssim 10^{-2}$ and thus the only component of current density $\boldsymbol{J}$ that makes a significant contribution to the Lorentz force is $\sigma\boldsymbol{E}$, which may be determined purely from the electric boundary conditions. A DC power supply can control the voltage across the sidewalls such that the total current I is set to a desired value at each time t. In this case, current rather than voltage is used as a control parameter, and the Lorentz force is appropriately expressed as

$$\boldsymbol{F} = \sigma(\boldsymbol{E} \times \boldsymbol{B}) = \frac{B_0 I(t)}{2\pi rh}\boldsymbol{e_\theta}, \tag{2.3}$$

neglecting any fringing of electric field lines due to the finite fluid depth (i.e. assuming that $\partial_z \boldsymbol{E} = 0$).

https://doi.org/10.1017/jfm.2024.674 Published online by Cambridge University Press

The resulting circulatory flow is governed by the incompressible equations of motion,

$$\partial_t \boldsymbol{u} + \boldsymbol{u}\cdot\boldsymbol{\nabla}\boldsymbol{u} = -\frac{1}{\varrho}\boldsymbol{\nabla} p + \nu\nabla^2\boldsymbol{u} + \frac{1}{\varrho}\boldsymbol{F}, \quad \boldsymbol{\nabla}\cdot\boldsymbol{u} = 0, \tag{2.4a,b}$$

where p is the deviation in pressure from the static pressure field $\varrho g(h-z)$.

We scale radial distances r by the outer sidewall radius r_o, vertical distances z by the fluid depth h and electric current I by its maximum value I_0, defining the non-dimensional quantities $\rho = r/r_o$, $\zeta = z/h$ and $\Upsilon = I/I_0$. A velocity scale U may be found by balancing the basal viscous drag ($\sim 2\nu U/h^2$) and Lorentz forces ($\sim B_0 I_0/[\pi h\varrho(r_i + r_o)]$) at the surface mid-gap, $z = h$, $r = (r_i + r_o)/2$:

$$U = \frac{B_0 I_0 h}{2\pi\nu\varrho(r_i + r_o)}. \tag{2.5}$$

This scale is used to produce the non-dimensional velocity $\boldsymbol{\upsilon} = \upsilon_\rho \boldsymbol{e_r} + \upsilon_\theta \boldsymbol{e_\theta} + (h/r_o)\upsilon_\zeta \boldsymbol{e_z}$, with components $\upsilon_\rho = u_r/U$, $\upsilon_\theta = u_\theta/U$ and $\upsilon_\zeta = (r_o/h)u_z/U$. An inertial scale ϱU^2 is used to non-dimensionalise reduced pressure as $\Pi = p/(\varrho U^2)$. Time is non-dimensionalised as $\tau = t/T$ by a surface mid-gap advective time scale:

$$T = \frac{r_i + r_o}{U}. \tag{2.6}$$

In sum, our non-dimensionalisation makes the mapping

$$(\boldsymbol{u}, p, I)(r, \theta, z, t) \mapsto (\boldsymbol{\upsilon}, \Pi, \Upsilon)(\rho, \theta, \zeta, \tau). \tag{2.7}$$

We introduce an *a priori* control Reynolds number Re and a magnetic Reynolds number Rm,

$$Re = \frac{h^2/\nu}{T} = \frac{B_0 I_0 h^3}{2\pi\nu^2\varrho(r_i + r_o)^2} \quad \text{and} \quad Rm = \frac{h^2/\eta}{T} = \frac{\nu}{\eta}Re, \tag{2.8a,b}$$

where $\eta = (\mu_0\sigma)^{-1}$ is the fluid's magnetic diffusivity and μ_0 is the magnetic permeability of free space. For $Rm \ll 1$, magnetic diffusion dominates over advection, and the quasi-static description of the Lorentz force (2.3) is valid (e.g. Knaepen & Moreau 2008; Favier *et al.* 2011; Davidson 2016; Verma 2017). As defined, $Rm \lesssim 10^{-10}$ for our experiments.

Also relevant are the radius ratio $\mathcal{R}$, aspect ratio $\mathcal{H}$ and depth-to-gap-width ratio Γ:

$$\mathcal{R} = r_i/r_o, \quad \mathcal{H} = h/r_o, \quad \text{and} \quad \Gamma = h/(r_o - r_i) = \mathcal{H}/(1-\mathcal{R}). \tag{2.9a–c}$$

Symbols for all dimensional parameters are listed in table 1. Definitions of scales and non-dimensional parameters are collected in table 2. The full non-dimensional axisymmetric equations in scaled cylindrical coordinates (ρ, θ, ζ) may be found in Appendix A.

We assume vertical hydrostasy, $0 = \partial_\zeta \Pi$, and cyclostrophic balance, $\upsilon_\theta^2/\rho = \partial_\rho \Pi$, achieved via deflection of the free surface. Under these conditions, the meridional flow $\boldsymbol{\upsilon}_\perp = \upsilon_\rho \boldsymbol{e_r} + \mathcal{H}\upsilon_\zeta \boldsymbol{e_z}$ vanishes, leaving a linear equation for azimuthal magneto-Stokes

https://doi.org/10.1017/jfm.2024.674 Published online by Cambridge University Press

Symbol	Description
r_i, r_o	Inner and outer sidewall radii (m)
h	Depth of fluid (m)
g	Gravitational acceleration (m s^{-2})
ν	Kinematic viscosity (m^2 s^{-1})
ϱ	Density (kg m^{-3})
σ	Electrical conductivity (S m^{-1})
γ	Surface tension (N m^{-1})
κ_c	Tracer diffusivity (m^2 s^{-1})
μ_0	Magnetic permeability of free space (kg m s^{-2} A^{-2})
I_0	Maximum electric current amplitude (A)
B_0	Magnetic flux density (magnitude) (T)
δ_i, δ_o, δ_b	95 % thickness of inner, outer, and basal boundary layers (m), defined in (2.23*a*,*b*), (2.28)

Table 1. Dimensional parameter definitions. Values are given in § 3.

Symbol	Definition	Eq.	Description
U	$B_0 h I_0/[2\pi\nu\varrho(r_i+r_o)]$	(2.5)	Shallow-layer velocity scale (m s^{-1})
U_{deep}	$B_0 I_0 (r_o-r_i)^2/[8\pi h\nu\varrho(r_i+r_o)]$	(2.25)	Deep-layer velocity scale (m s^{-1})
$u_{\theta,mid\text{-}gap}$	$U\bar{v}_\theta(\rho=(1+\mathcal{R})/2,\zeta=1)$	(2.24)	Surface mid-gap value of steady solution (2.16) (m s^{-1})
T	$(r_i+r_o)/U$	(2.6)	Advective time scale (s)
T_{su}	$4h^2/(\pi^2\nu)$	(2.19)	Spin-up time scale (s)
T_{circ}	$\pi(r_i+r_o)/u_{\theta,mid\text{-}gap}$	(5.19)	Surface mid-gap circulation time (s)
Ha	$B_0 h\sqrt{\sigma_0/(\varrho\nu)}$	(2.2)	Hartmann number
Re	$h^2/(\nu T)=B_0 I_0 h^3/[2\pi\varrho\nu^2(r_i+r_o)^2]$	(2.8*a*)	Control Reynolds number
Rm	$\nu\mu_0\sigma_0 Re$	(2.8*b*)	Magnetic Reynolds number
Fr	$U/\sqrt{gh}$	(2.13)	Froude number
Bo	$\varrho g h^2/\gamma$	(2.14)	Bond number
$\mathcal{R}$	r_i/r_o	(2.9*a*)	Sidewall radius ratio
$\mathcal{H}$	h/r_o	(2.9*b*)	Aspect ratio
Γ	$h/(r_o-r_i)$	(2.9*c*)	Depth-to-gap-width ratio
Δ_i, Δ_o, Δ_b	$\delta_i/(r_o-r_i)$, $\delta_o/(r_o-r_i)$, δ_b/h	(2.23*a*,*b*), (2.28)	Inner, outer and basal boundary layer thicknesses
Sc	ν/κ_c	(5.9*a*)	Schmidt number
Pe	$ScRe=h^2/(\kappa_c T)$	(5.9*b*)	Péclet number
Pe_{circ}	$u_{\theta,mid\text{-}gap} r_o^2/(U\pi h^2)\,Pe=r_o^2/(\kappa_c T_{circ})$	(5.20)	Circulation Péclet number
$\widetilde{Pe}$	$(2\pi(1+\mathcal{R})^2/\mathcal{H}^3)\,Pe=B_0 I_0 r_o/(\varrho\nu\kappa_c)$	(5.21)	Electromagnetic forcing Péclet number

Table 2. Scales and non-dimensional parameters. All quantities below the dashed line are non-dimensional.

flow,

$$Re\,\partial_\tau v_\theta = \nabla_\perp^2 v_\theta - \mathcal{H}^2\frac{v_\theta}{\rho^2} + \frac{\mathcal{R}+1}{\rho}\Upsilon(\tau), \tag{2.10}$$

where we have defined the operator

$$\nabla_\perp^2(\cdot) = \left[\mathcal{H}^2\rho^{-1}\partial_\rho\rho\partial_\rho + \partial_\zeta^2\right](\cdot). \tag{2.11}$$

https://doi.org/10.1017/jfm.2024.674 Published online by Cambridge University Press

We consider the rectangular domain $(\rho, \zeta) \in (\mathcal{R}, 1) \times (0, 1)$ with boundary conditions

$$\upsilon_\theta(\mathcal{R}, \zeta, \tau) = \upsilon_\theta(1, \zeta, \tau) = \upsilon_\theta(\rho, 0, \tau) = \left[\partial_\zeta \upsilon_\theta\right]_{\zeta=1} = 0. \tag{2.12}$$

This approximation to the free-surface boundary conditions is appropriate as long as the deflection due to capillary action and centrifugation is negligible (e.g. Greenspan & Howard 1963). The Froude number Fr compares the deflection of the free surface due to centrifugation ($\sim U^2 g^{-1}$) with the depth of the fluid (h):

$$Fr = \sqrt{U^2 g^{-1}/h}. \tag{2.13}$$

Surface deflection due to capillary rise or dewetting is characterised by the capillary length (e.g. Martino *et al.* 2006), $l = \sqrt{\gamma/(\varrho g)}$. The Bond number Bo compares this length scale with the fluid depth:

$$Bo = (h/l)^2 = \varrho g h^2/\gamma. \tag{2.14}$$

In our validation experiments, $Fr \lesssim 10^{-2}$ and $Bo \geqslant 4.4$, so we adopt (2.12).

2.2. *Spin up from rest*

Solutions to (2.10), (2.12) that develop from an initially quiescent fluid ($\upsilon_\theta = 0$ at $\tau = 0$) once constant electric current is applied ($\Upsilon = 1$ for $\tau > 0$) may be expressed as

$$\upsilon_\theta(\rho, \zeta, \tau) = \bar{\upsilon}_\theta(\rho, \zeta) + \upsilon'_\theta(\rho, \zeta, \tau). \tag{2.15}$$

The stationary component is

$$\bar{\upsilon}_\theta(\rho, \zeta) = \left(\frac{\mathcal{R}+1}{2}\right)\frac{2\zeta - \zeta^2}{\rho} - \sum_{n=1}^{\infty} \frac{2(\mathcal{R}+1)}{k_n^2 \mathcal{H}}\left[A_n \mathrm{I}_1\left(\frac{k_n}{\mathcal{H}}\rho\right) + B_n \mathrm{K}_1\left(\frac{k_n}{\mathcal{H}}\rho\right)\right]\sin(k_n \zeta), \tag{2.16}$$

with

$$A_n = \frac{\mathcal{H}}{k_n \mathcal{R}}\left[\frac{\mathcal{R}\mathrm{K}_1(k_n\mathcal{R}/\mathcal{H}) - \mathrm{K}_1(k_n/\mathcal{H})}{\mathrm{I}_1(k_n/\mathcal{H})\,\mathrm{K}_1(k_n\mathcal{R}/\mathcal{H}) - \mathrm{K}_1(k_n/\mathcal{H})\,\mathrm{I}_1(k_n\mathcal{R}/\mathcal{H})}\right], \tag{2.17a}$$

$$B_n = \frac{\mathrm{I}_1(k_n/\mathcal{H}) - \mathcal{R}\mathrm{I}_1(k_n\mathcal{R}/\mathcal{H})}{\mathcal{R}\mathrm{K}_1(k_n\mathcal{R}/\mathcal{H}) - \mathrm{K}_1(k_n/\mathcal{H})} A_n, \tag{2.17b}$$

where I_1 and K_1 denote modified Bessel functions of the first and second kind, respectively, and $k_n = \pi(n - 1/2)$.

The exact form of the time-dependent component $\upsilon'_\theta(\rho, \zeta, \tau)$ is provided in Appendix A, but is well approximated for shallow layers ($\Gamma \ll 1$) by

$$\upsilon'_\theta(\rho, \zeta, \tau) \approx -\bar{\upsilon}_\theta(\rho, \zeta)\exp\left(-\frac{T\tau}{T_{su}}\right), \tag{2.18}$$

where the characteristic time scale for spin up from rest is

$$T_{su} = \frac{4Re}{\pi^2}T = \frac{4h^2}{\pi^2 \nu}. \tag{2.19}$$

https://doi.org/10.1017/jfm.2024.674 Published online by Cambridge University Press

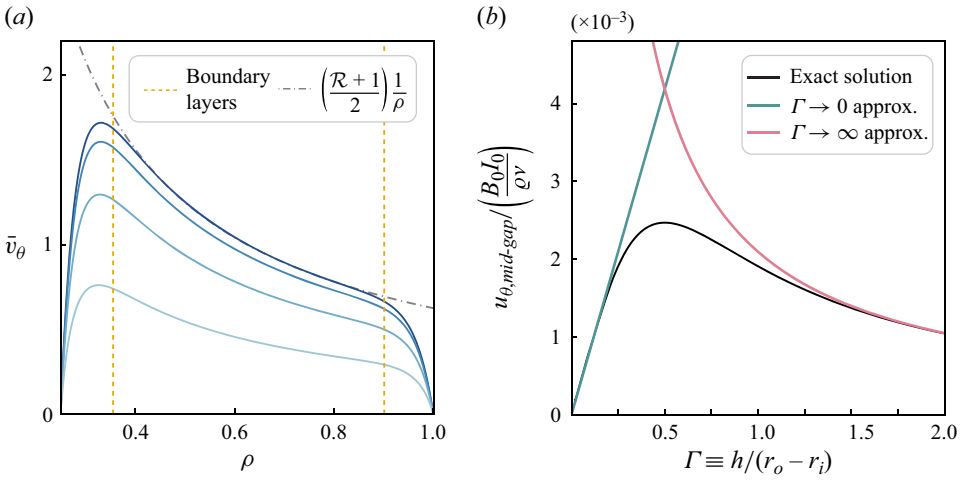


Figure 2. (*a*) Stationary magneto-Stokes flow solution given by (2.16) for a channel with geometric ratios $\mathcal{H} = 0.05$ and $\mathcal{R} = 0.25$. Labelled contours trace the solution profile at different heights ζ above the channel base. A dash-dotted grey line shows the solution in the shallow limit ($\Gamma \to 0$), and yellow dashed lines correspond to the 95 % thicknesses of the sidewall boundary layers. (*b*) Magnitude of the surface mid-gap velocity as a function of depth-to-gap-width ratio Γ for a channel with $\mathcal{R} = 0.9$. The exact solution (black) is computed using (2.16). The curves corresponding to shallow- (teal) and deep-layer (pink) asymptotic solutions are plotted using (2.20) and (2.26), respectively.

2.3. *Shallow- and deep-layer regimes*

The first term in (2.16) is equal to the asymptotic solution in the shallow-layer limit $\Gamma \to 0$:

$$\lim_{\Gamma\to 0} \bar{v}_\theta = \left(\frac{\mathcal{R}+1}{2}\right)\frac{2\zeta - \zeta^2}{\rho}, \tag{2.20}$$

which inherits the inverse dependence on radius of the Lorentz force (since $\|\boldsymbol{J}\| \propto 1/r$). The surface velocity profile is then identical to Taylor–Couette flow with inner and outer sidewall rotation rates given by

$$\Omega_i = \frac{B_0 I(t) h}{4\pi\varrho\nu r_i^2} \quad \text{and} \quad \Omega_o = \frac{B_0 I(t) h}{4\pi\varrho\nu r_o^2}, \tag{2.21a,b}$$

and naturally shares Taylor–Couette flow's kinematic reversibility for $Re \ll 1$ (Taylor 1967).

For $\mathcal{H} > 0$, the series in (2.16) produces boundary layers at both sidewalls with 95 % thicknesses δ_i, δ_o defined such that

$$\bar{v}_\theta = 0.95 \lim_{\Gamma\to 0} \bar{v}_\theta \quad \text{at } \rho = (r_i + \delta_i)/r_o,\ (r_o - \delta_o)/r_o, \quad \zeta = 1. \tag{2.22}$$

Figure 2(*a*) shows the stationary solution given by (2.16) for a channel with geometric ratios $\mathcal{H} = 0.05$ and $\mathcal{R} = 0.25$. Contours correspond to different vertical positions ζ within the fluid, and dashed yellow lines indicate the 95 % thicknesses of the sidewall boundary layers. The size of each boundary layer relative to the channel width scales as

$$\Delta_i \equiv \frac{\delta_i}{r_o - r_i} \approx 2.51\Gamma^{1.08}, \quad \Delta_o \equiv \frac{\delta_o}{r_o - r_i} \approx 2.11\Gamma^{1.06}. \tag{2.23a,b}$$

All numerical factors and powers in (2.23*a*,*b*) are fit to values of Δ_i, Δ_o computed from (2.16) for $0.01 \leqslant \mathcal{H} \leqslant 0.3$ and $0.01 \leqslant \mathcal{R} \leqslant 0.99$.

https://doi.org/10.1017/jfm.2024.674 Published online by Cambridge University Press

The scalings (2.23*a*,*b*) predict a shallow-layer regime in which sidewall boundary layers are distinct (i.e. $\Delta_i + \Delta_o < 1$) for $\Gamma \lesssim 0.24$. This regime is also characterised by the growth of the mid-gap velocity magnitude

$$u_{\theta,mid\text{-}gap} = U\bar{v}_\theta(\rho = \mathcal{R}/2 + 1/2, \zeta = 1), \tag{2.24}$$

with layer depth h necessary for the basal viscous drag ($\sim 2\nu U/h^2 \propto Uh^{-2}$) to balance the Lorentz force ($\sim B_0 I_0/[\pi h\varrho(r_i + r_o)] \propto h^{-1}$). Figure 2(*b*) shows the growth of $u_{\theta,mid\text{-}gap}$ (black curve) with layer depth closely following the linear dependence predicted by the asymptotic shallow-layer solution (2.20) (teal curve) for $\Gamma \lesssim 0.24$.

If the layer depth is increased (while still keeping inertial forces small, $Re \ll 1$), the dominant balance of Lorentz and sidewall viscous drag forces ($\sim 8\nu U_{deep}/[r_o - r_i]^2$) leads to an alternate velocity scale

$$U_{deep} = \frac{B_0 I_0 (r_o - r_i)^2}{8\pi h \nu \varrho (r_i + r_o)} = \frac{U}{4\Gamma^2}. \tag{2.25}$$

Using U_{deep} to non-dimensionalise velocity as $w_\theta = u_\theta / U_{deep}$, the steady solution for an infinitely deep channel is

$$\lim_{\Gamma\to\infty} \bar{w}_\theta = \frac{2\left(1-\rho^2\right)\mathcal{R}^2 \log(\mathcal{R}) - 2\left(1-\mathcal{R}^2\right)\rho^2 \log(\rho)}{(1-\mathcal{R})^3 \rho}. \tag{2.26}$$

See Gleeson *et al.* (2004) for the dimensional form of (2.26).

For deep channels of finite depth ($0.24 \lesssim \Gamma < \infty$), flow is invariant with height outside of a basal boundary layer with 95 % thickness δ_b defined such that

$$\bar{w}_\theta = 0.95 \lim_{\Gamma\to\infty} \bar{w}_\theta \quad \text{at } \rho = (1+\mathcal{R})/2, \quad \zeta = \delta_b/h. \tag{2.27}$$

The relative thickness scales as

$$\Delta_b \equiv \delta_b/h \approx 0.831\,\Gamma^{-0.961}. \tag{2.28}$$

The numerical factor and power in (2.28) are fit to values of Δ_b computed from (2.16) for $1 \leqslant \mathcal{H} \leqslant 20$ and $0.01 \leqslant \mathcal{R} \leqslant 0.99$.

We may then define a deep-layer regime with the condition $\Delta_b < 0.2$, satisfied for $\Gamma \gtrsim 4.4$. This regime is also characterised by the decrease of $u_{\theta,mid\text{-}gap}$ with layer depth, since the dependence of $u_{\theta,mid\text{-}gap}$ on h is mainly controlled by the Lorentz force ($\propto h^{-1}$). Figure 2(*b*) shows the change in $u_{\theta,mid\text{-}gap}$ (black curve) with layer depth closely following the inverse dependence predicted by the asymptotic deep-layer solution (2.26) (pink curve) for $\Gamma > 1$.

Figure 3(*a*) uses the conditions $\Delta_i + \Delta_o < 1$ and $\Delta_b < 0.2$ with the scalings (2.23*a*,*b*), (2.28) to demarcate shallow- and deep-layer regimes in the space of aspect and radius ratios. Teal, purple and pink dots in figure 3(*a*) correspond to shallow-layer, transitional and deep-layer flows in channels of the same radius ratio $\mathcal{R} = 0.9$, whose predicted radial and vertical profiles are plotted in panels (*b*,*c*), respectively. Asymptotic shallow- and deep-layer solutions (2.20), (2.26) are plotted as dashed curves.

3. Experimental methods

We validate the approximate solution (2.15) via four laboratory experiments (cases I–IV), matched with DNS of the nonlinear axisymmetric flow governed by (A1), (A2).

https://doi.org/10.1017/jfm.2024.674 Published online by Cambridge University Press

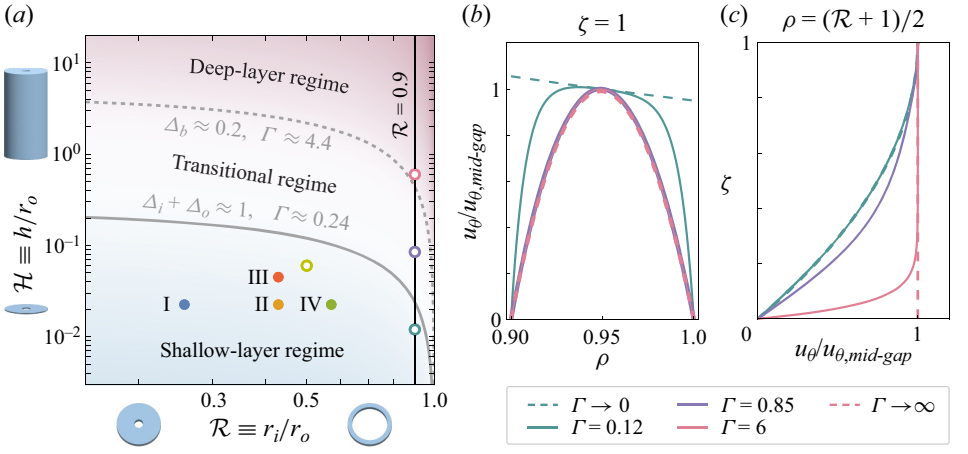


Figure 3. (*a*) Regime diagram for annular magneto-Stokes flow in the space of radius ratios $\mathcal{R}$ and aspect ratios $\mathcal{H}$. Renderings of cylindrical annuli correspond to axes values. Background tones grade from cool to warm with increasing Γ. A solid grey line indicates the boundary $\Delta_i + \Delta_o \approx 1$ (predicted by (2.23*a*,*b*)) between shallow-layer and transitional regimes, while a dashed grey line indicates the boundary $\Delta_b \approx 0.2$ (predicted by (2.28)) between transitional and deep-layer regimes. Points labelled with roman numerals correspond to laboratory cases discussed in §§ 3, 4. Open markers correspond to DNS cases discussed in § 5.2. (*b*) A comparison of magneto-Stokes flows in channels of varying depth-to-gap-width ratio Γ at a fixed radius ratio $\mathcal{R} = 0.9$. Plotted are radial profiles of surface azimuthal velocity predicted from theory (2.16) and scaled by surface values at the channel centre, $u_{\theta,mid\text{-}gap}$. Solid curves correspond to open markers of the same colour in the regime diagram (panel *a*). Dashed teal and pink curves show the corresponding shallow (2.20) and deep (2.26) asymptotic solutions, respectively.

This complementary approach permits us to test various physical effects not accounted for in our model: the DNS test the impact of meridional flow alone, while the laboratory experiments add the effects of surface tension and a dynamic free surface. The results of these validation cases are discussed in § 4. An additional laboratory experiment (case HS) is detailed in § 5.

3.1. *Laboratory experiments*

Validation experiments (cases I–IV) are performed using an open-top annular channel consisting of a 17.5 cm-radius steel outer cylindrical sidewall, acrylic base and a removable stainless steel inner cylindrical sidewall, which may be replaced with cylinders of different radii. The channel is placed inside the solenoidal electromagnet bore of UCLA's RoMag device (Xu, Horn & Aurnou 2022), and a DC bench power supply provides a controlled current I between the channel sidewalls. An 80.0 ± 0.05 g l^{-1} NaCl : H_2O solution is used as the working fluid for all cases; 0.1 ml of dish detergent is added for every litre of solution to reduce surface tension, which is measured as $\gamma = 38 \pm 4$ mN m^{-1} using the capillary rise method (e.g. Martino *et al.* 2006). The fluid is estimated to have electrical conductivity $\sigma = 12.3 \pm 0.1$ S m^{-1}, kinematic viscosity $\nu = (1.10 \pm 0.05) \times 10^{-6}$ m^2 s^{-1} and density $\varrho = 1059.1 \pm 0.7$ kg m^{-3}, using the salinity-based models of Park (1964), Isdale, Spence & Tudhope (1972) and Isdale & Morris (1972), respectively.

Inner radius, fluid height, electric current and magnetic field strength are varied across cases I–IV; values of these dimensional parameters are reported in table 3. Cases I–IV span three different radius ratios $\mathcal{R} = 0.25, 0.44, 0.58$ and two different aspect ratios $\mathcal{H} = 0.023, 0.046$; these values correspond to the solid points in figure 3(*a*). Fluid depth is kept

https://doi.org/10.1017/jfm.2024.674 Published online by Cambridge University Press

Case	I_0 (a) (± 0.003 A)	B_0 (mT)	h (cm) (± 0.05 cm)	r_i (cm) (± 0.03 cm)	r_o (cm) (± 0.03 cm)	U (cm s^{-1})
I	0.081	30.0 ± 0.2	0.4	4.44	17.52	0.56 ± 0.08
II	0.099	30.0 ± 0.6	0.4	7.62	17.52	0.63 ± 0.09
III	0.039	20.0 ± 0.4	0.8	7.62	17.52	0.36 ± 0.04
IV	0.099	35 ± 1	0.4	10.14	17.52	0.7 ± 0.1
HS	0.060	190 ± 1	0.2	3.75	9.84	0.24 ± 0.06

Table 3. Dimensional experimental parameters and predicted velocity U at surface mid-gap ($z = h$, $r = [r_i + r_o]/2$), computed using (2.5). Error in values of U reflect the propagation of measurement uncertainty of the control parameters.

Case	$\mathcal{R}$	$\mathcal{H}$	Re	Fr	Bo	Ha	Rm
I	0.25	0.023	0.38	0.030	4.4	0.012	6.6×10^{-12}
II	0.44	0.023	0.36	0.032	4.4	0.012	6.3×10^{-12}
III	0.44	0.046	0.78	0.012	18	0.016	1.3×10^{-11}
IV	0.58	0.023	0.35	0.034	4.4	0.014	6.1×10^{-12}
HS	0.38	0.020	0.058	0.016	1.1	3.8×10^{-3}	1.0×10^{-12}

Table 4. Non-dimensional experimental parameters. The radius ratio $\mathcal{R}$, aspect ratio $\mathcal{H}$, control Reynolds number Re, Froude number Fr, Bond number Bo, Hartmann number Ha and magnetic Reynolds number Rm are defined in § 2.

above the capillary length $l = 0.19 \pm 0.01$ cm ($Bo > 1$) to minimise relative differences in depth due to capillary action. Voltage across the electrodes is maintained under $\sim$1.5 V to prevent electrolysis of water. Under this constraint, electric current and magnetic field strength are held between 0.04 and 0.1 A and 20 and 35 mT, respectively, to keep $Re < 1$ and $Fr^2 \ll 1$. Values of these non-dimensional control parameters are reported in table 4.

Before the start of each case (I–IV), a streak of buoyant blue dye is drawn across the quiescent fluid surface. From $t = 0$ to $t = 0.5\pi T$, the power supply drives a constant current I_0, and an overhead camera records the dye advection. Blue-channel thresholding and Canny edge detection (Canny 1986; Bradski 2000) are applied to the perspective-corrected video in order to track the (Lagrangian) angular position $\theta(r, t)$ of the leading dye streak edge. Uncertainty in $\theta(r, t)$ is computed as the change in estimated position under a 10 % adjustment of colour threshold values. At every $\Delta t = 0.5T_{su}$, θ is determined at 15 points across the channel (in r), excluding the menisci at the sidewalls where dye spreads rapidly via adhesion instead of advection. A time series of surface velocity $u_\theta(r)$ is then estimated via second-order central difference of $\theta(r, t)$ over time.

3.2. *Direct numerical simulations*

Cases I–IV are matched with DNS of nonlinear, axisymmetric flow governed by (A1), (A2) with initially quiescent flow ($\boldsymbol{\upsilon} = 0$ at $\tau = 0$, $\Upsilon = 1$ for $\tau > 0$) and no-slip conditions on all boundaries except for the surface, which is treated as a free-slip rigid lid: $\boldsymbol{\upsilon}(\mathcal{R}, \zeta, \tau) = \boldsymbol{\upsilon}(1, \zeta, \tau) = \boldsymbol{\upsilon}(\rho, 0, \tau) = 0$, $[\partial_\zeta \upsilon_\rho]_{\zeta=1} = [\partial_\zeta \upsilon_\theta]_{\zeta=1} = \upsilon_\zeta(\rho, 1, \tau) = 0$. We employ the Dedalus pseudospectral framework (Burns *et al.* 2020), expanding υ_ζ in 512 sine modes in ζ and all other fields in 512 cosine modes in ζ; all fields are expanded in ρ with 256 Chebyshev modes. The no-slip condition is enforced at $\zeta = 0$ using the volume-penalty method (Hester, Vasil & Burns 2021), which adds spatially masked linear damping terms

https://doi.org/10.1017/jfm.2024.674 Published online by Cambridge University Press

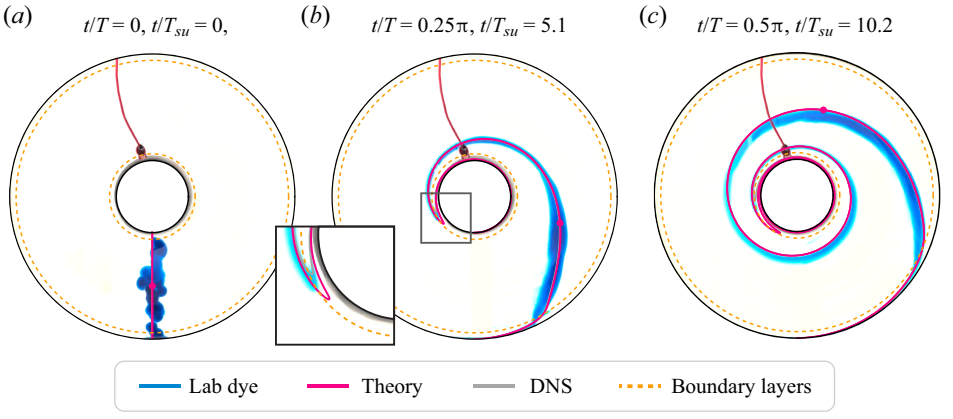


Figure 4. Snapshots of a free-surface dye track (blue) from laboratory case I, (*a*) when power is turned on, (*b*) after ∼5 spin up times and (*c*) after ∼10 spin up times. Time integrations of the approximate analytical solution (2.15) and DNS result are overlain as magenta and grey curves, respectively. Dotted yellow circles correspond to the 95 % thickness of each sidewall boundary layer as predicted from (2.15). The red cord near the 12 o'clock position in each photograph is the electrical wire leading from the power supply to the inner electrode.

$-G(\zeta/\delta)u_\rho/\tau_{VP}$, $-G(\zeta/\delta)u_\theta/\tau_{VP}$, $-G(\zeta/\delta)u_\zeta/\tau_{VP}$ to the corresponding components of the axisymmetric momentum equation (A1), where $G(x) = [1 - \mathrm{erf}(\sqrt{\pi}x)]/2$ is a masking function and τ_{VP} is the volume-penalty damping time scale non-dimensionalised by T. The masking function is smoothed over a vertical length scale δ (set here to $\delta = 0.01$), which is used to determine an appropriate value for τ_{VP}. This is effected by requiring the damping length scale $\sqrt{\tau_{VP}/Re}$ to be proportional to the smoothing scale: $\sqrt{\tau_{VP}/Re} = \delta/\delta^*$. The proportionality constant δ^* is set to the optimal value found by Hester *et al.* (2021), $\delta^* = 3.11346786$; this choice of δ^* eliminates the displacement length error associated with the mask, $G(x)$. See Hester *et al.* (2021) for details on optimising the volume-penalty method.

In all simulations, the system is integrated from $\tau = 0$ to $\tau = 1.1\pi$ over 10^4 time steps using the second-order semi-implicit backwards difference (SBDF2) scheme (Wang & Ruuth 2008, (2.8)). Acceleration, pressure and rectilinear viscous terms are time integrated implicitly; the remaining terms are treated explicitly.

Reported results match those obtained at half their spatial resolution as well as the analytical solution at $t = 3T_{su}$. The code used for these simulations and for the dye-tracking described in § 3.1 is available online (https://github.com/cysdavid/magnetoStokes).

4. Results

Figure 4 shows three photographs of laboratory case I, taken when power is turned on (*a*), after 0.25 circulation times (*b*) and after 0.5 circulation times (*c*). The time-integrated analytical solution (2.15) and DNS results are overlain in magenta and grey, respectively. Laboratory, analytical and numerical results match well in the bulk, differing most within the boundary layers (dashed yellow lines). A close up (*b*, inset) of the inner boundary layer shows the laboratory dye streak and DNS curve trailing behind the analytical solution, resulting from the parasitic effect of meridional circulation on the steady-state azimuthal flow and from a lag in spin-up. The bulk flow also exhibits finite spin-up time effects. In

https://doi.org/10.1017/jfm.2024.674 Published online by Cambridge University Press

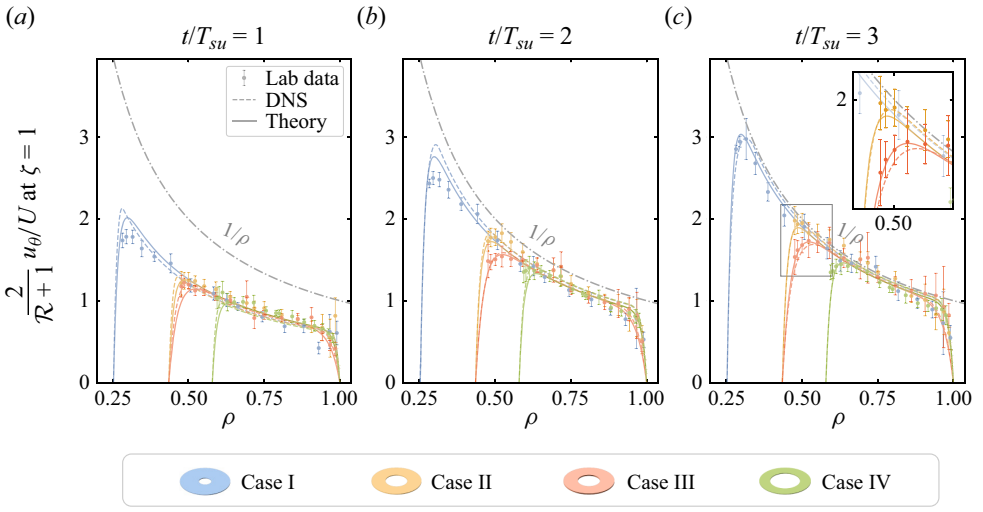


Figure 5. Radial profiles of scaled azimuthal velocity at the free surface for cases I–IV at (*a*) 1 spin-up time after rest, (*b*) 2 spin-up times and (*c*) 3 spin-up times. Solid theoretical curves are computed using (2.15). The DNS are shown via dashed curves. Also plotted is the $1/\rho$ profile (dash-dotted grey curve) corresponding to the shallow ($\Gamma \to 0$), long-time solution (2.20) at $\zeta = 1$. Error bars represent ± 1 standard deviation propagated from uncertainty in the dye-tracking velocimetry algorithm and from uncertainty in the predicted velocity scale U used to normalise the data. Rendered cylindrical annuli in the lower legend depict the channel geometry of each case.

each panel of figure 4, a magenta dot is placed on the analytical curve at $r = (r_i + r_o)/2$. For flow that has fully spun up, πT is the time it takes for this dot to make one revolution. In figure 4(*b*), the magenta dot has travelled slightly less than a quarter revolution from $t = 0$ to $t = 0.25\pi T$, a product of the finite *Re* value in our experiments.

Figure 5 plots radial profiles of scaled azimuthal velocity for all four cases. Included are laboratory data (points), DNS results (dashed curves) and the approximate analytical solution given by (2.15) (solid curves) after 1 spin-up time (*a*), 2 spin-up times (*b*) and 3 spin-up times (*c*). Bars on the data points correspond to error introduced by the dye-tracking algorithm and from measurement uncertainty propagated through the computed velocity scale U. The scaled velocity profiles evolve towards the $1/\rho$ curve (grey dash-dotted line) over time, apart from the boundary layers. A close up of the inner boundary layer for the two cases with $\mathcal{R} = 0.44$ (panel *c*, inset) shows a clear separation between the profiles for $\mathcal{H} = 0.023$ (case II) and $\mathcal{H} = 0.046$ (case III) and excellent agreement with theory.

A slight separation between data, DNS, and theory at case I's peak in velocity (near $\rho = 0.3$) for $t/T_{su} \leqslant 2$ can be seen in figure 5(*a*,*b*). The laboratory flow (blue points) spins up slower than the approximate solution (solid blue line), while the DNS result (dashed blue line) spins up faster. The gap between laboratory data and theory may be related to the dynamic adjustment of the free surface or the reduction of current density at sidewall menisci. In contrast, the gap between theory and DNS is largely the result of the sidewall viscous drag's effect on spin-up. As evident in the full solution in Appendix A, features with higher spatial frequency in the radial direction (e.g. the sharp peak near $\rho = 0.3$) spin up faster than lower frequency features. This effect is neglected in the approximate solution (2.15) but is retained in the DNS.

These finite-*Re* simulations also retain nonlinear advection, and each DNS case exhibits a steady (for $t \gg T_{su}$) clockwise vortex in the ρ, ζ-plane near the inner sidewall where

https://doi.org/10.1017/jfm.2024.674 Published online by Cambridge University Press

centrifugal forces are strongest (cf. Norouzi & Biglari 2013). This meridional circulation has a parasitic effect on the azimuthal flow, resulting in the slight gap between DNS and theory in figure 5(*c*). The largest root mean square error between theory and DNS (case I) is 3.3 % of the average DNS azimuthal velocity at $t = 3T_{su}$. This difference is smaller than the error bars on the laboratory data and is expected to vanish with decreasing Re.

5. Low-Re mixing in magneto-Stokes flow

The expansion of 'lab on a chip' technology across a range of industrial and biomedical fields has increased demand for microfluidic devices that can efficiently mix chemical species at low Re (Pamme 2006; Mansur *et al.* 2008; Jeong *et al.* 2010). Magneto-Stokes systems (Yi, Qian & Bau 2002; West *et al.* 2003; Gleeson *et al.* 2004) are particularly well suited to this purpose because they have no moving components that require miniaturisation and they work in simple, easily fabricated channel geometries (cf. Ehrfeld *et al.* 1999; Bertsch *et al.* 2001).

In the following subsections, we analyse the properties of magneto-Stokes flow relevant to low-Re mixing. The design of efficient micromixers often focuses on the generation of vortices (Sudarsan & Ugaz 2006; Chang & Yang 2007 and reference therein), which tend to augment mixing (e.g. Cetegen & Mohamad 1993). Therefore, in § 5.1, we determine the conditions under which the Lorentz force can produce vorticity in shallow-layer magneto-Stokes flows in arbitrary (2-D) channel geometry. In micromixers that drive flow via electroosmosis rather than MHD, the generation of vorticity hinges on breaking the similitude between velocity and the electric field (Cummings *et al.* 2000). An analogous similitude property exists for many magneto-Stokes flows, including our annular configuration, for which the 2-D velocity field and the Lorentz force are everywhere proportional by the same amount. In contrast to electroosmotic flows, annular magneto-Stokes flow is irrotational even when obstacles are placed in the channel to break similitude (cf. the obstacle-induced electroosmotic vortices in Dukhin 1991; Ben & Chang 2002).

We show in § 5.2 that, despite the lack of significant axial vorticity, shallow-layer annular magneto-Stokes flow enhances mixing via Taylor dispersion (Taylor 1953; Aris 1956) or through an advectively dominated mechanism similar to that of a point-vortex flow (Rhines & Young 1983; Flohr & Vassilicos 1997). Our results extend to transitional and deep-layer flows, and they demonstrate that shear enhancement of mixing is initiated for the least electromagnetic effort ($B_0 I_0$) in $\Gamma \approx 1$ channels.

5.1. *Irrotationality in shallow-layer magneto-Stokes systems*

We consider a magneto-Stokes micromixer of uniform depth h and arbitrary planform (i.e. lateral boundary geometry) placed in a vertical magnetic field $\boldsymbol{B} = B_z \boldsymbol{e_z}$. The governing equation (2.10) generalises to

$$Re\,(\partial_\tau \boldsymbol{v} + \boldsymbol{v}\cdot\boldsymbol{\nabla}_{2D}\boldsymbol{v}) = -\boldsymbol{\nabla}_{2D}P + \mathcal{H}^2\nabla_{2D}^2\boldsymbol{v} + \partial_\zeta^2\boldsymbol{v} + \boldsymbol{f}, \quad \boldsymbol{\nabla}_{2D}\cdot\boldsymbol{v} = 0, \qquad (5.1a,b)$$

where we now permit non-axisymmetry and lateral pressure gradients but retain vertical hydrostasy ($\boldsymbol{v}\cdot\boldsymbol{e_z} = 0$). Here, we have altered the non-dimensionalisation in § 2.1 to use a generic horizontal length scale L in place of r_o, r_i, and defined $\boldsymbol{\nabla}_{2D}$ such that $\boldsymbol{\nabla}(\cdot) = h^{-1}[\mathcal{H}\boldsymbol{\nabla}_{2D} + \boldsymbol{e_z}\partial_\zeta](\cdot)$. Dimensionless pressure P and horizontal Lorentz force $\boldsymbol{f}$ have been scaled with $\varrho\nu ULh^{-2}$ and $\varrho\nu Uh^{-2}$, respectively.

In the limits $Re, \mathcal{H} \to 0$, appropriate for lab-on-a-chip systems, we make a Hele-Shaw approximation (Hele-Shaw 1898) motivated by the form of the annular shallow-layer

https://doi.org/10.1017/jfm.2024.674 Published online by Cambridge University Press

solution (2.20): $\boldsymbol{v} = (2\zeta - \zeta^2)\boldsymbol{v}_{2D}$ where $\partial_\zeta \boldsymbol{v}_{2D} = 0$. Applying these assumptions to (5.1*a*,*b*) yields

$$\boldsymbol{v}_{2D} = \tfrac{1}{2}\left(\boldsymbol{f} - \boldsymbol{\nabla}_{2D}P\right), \quad \boldsymbol{n}\cdot\boldsymbol{v}_{2D} = 0 \quad \text{on } \partial\mathcal{D}, \tag{5.2a,b}$$

where $\boldsymbol{n}$ denotes the unit vector normal to the lateral boundaries $\partial\mathcal{D}$. Then, the quasi-2-D flow is irrotational if and only if

$$\boldsymbol{e}_z\cdot(\boldsymbol{\nabla}_{2D}\times\boldsymbol{f}) = \frac{h^2\sigma}{\varrho\nu U}\left[B_z\partial_z E_z - (\boldsymbol{E}\cdot\boldsymbol{\nabla})\,B_z\right] = 0, \tag{5.3}$$

where we have used Gauss's law ($\partial_z B_z = 0$) and neglected free charges ($\boldsymbol{\nabla}\cdot\boldsymbol{E} = 0$). Thus, vorticity can be generated in a magneto-Stokes micromixer given strong vertical gradients in E_z or horizontal gradients in B_z.

Since the quasistatic electromagnetic fields can be prescribed, the resulting 2-D flow may be readily predicted using (5.2*a*,*b*) after solving the pressure equation,

$$\nabla^2_{2D}P = \boldsymbol{\nabla}_{2D}\cdot\boldsymbol{f}, \quad \boldsymbol{n}\cdot\boldsymbol{\nabla}_{2D}P = \boldsymbol{n}\cdot\boldsymbol{f} \quad \text{on } \partial\mathcal{D}. \tag{5.4a,b}$$

This problem is greatly simplified if the Lorentz force is non-divergent:

$$\boldsymbol{\nabla}_{2D}\cdot\boldsymbol{f} = \frac{h^2\sigma}{\varrho\nu U}\boldsymbol{E}\cdot(\boldsymbol{\nabla}\times\boldsymbol{B}) = 0, \tag{5.5}$$

and if the boundaries are perfectly conducting:

$$\boldsymbol{n}\times\boldsymbol{E} = 0 \quad \text{on } \partial\mathcal{D}, \tag{5.6}$$

such that $\boldsymbol{n}\cdot\boldsymbol{f} = 0$ on $\partial\mathcal{D}$. The relations (5.4*a*,*b*)–(5.6) imply $\boldsymbol{\nabla}_{2D}P = 0$ identically, which results in similitude between the prescribed Lorentz force and the resultant velocity field: $\boldsymbol{v}_{2D} = \frac{1}{2}\boldsymbol{f}$.

An analogous similitude exists for some electrokinetic flows, where the velocity is proportional to the applied electric field instead of the Lorentz force (Cummings *et al.* 2000). These electrokinetic flows are necessarily irrotational by nature of the quasistatic electric fields used to drive them, and thus the key to generating vorticity lies in breaking similitude (Dukhin 1991; Ben & Chang 2002). In contrast, 2-D magneto-Stokes flows are only irrotational if (5.3) is satisfied, which is independent of the similitude conditions (5.5), (5.6). Thus, magneto-Stokes micromixers can benefit simultaneously from the presence of vorticity and the analytical convenience of similitude between the velocity and imposed Lorentz force.

If (5.3), (5.5) and (5.6) are all satisfied, as is the case for the annular device considered in this work, then the Lorentz force and velocity are proportional to the gradient of a potential Φ that is possibly multi-valued (like that of a point vortex; Lamb 1906). Potential flow is maintained even when similitude is broken (e.g. by the addition of an electrically insulating obstacle to the flow). The only change is the contribution of pressure to the total potential:

$$\boldsymbol{v}_{2D} = \tfrac{1}{2}\boldsymbol{\nabla}_{2D}\left(\Phi - P\right). \tag{5.7}$$

The pressure field P may be constructed to enforce the no-flux condition on the lateral boundaries using potential theory (e.g. Lamb 1906; Milne-Thomson 1938).

In practice, these magneto-Stokes potential flows readily arise even with moderate gradients in magnetic field strength and fringing of electric field lines near menisci. Figure 6 shows magneto-Stokes flow around an electrically insulating plastic obstacle in

https://doi.org/10.1017/jfm.2024.674 Published online by Cambridge University Press

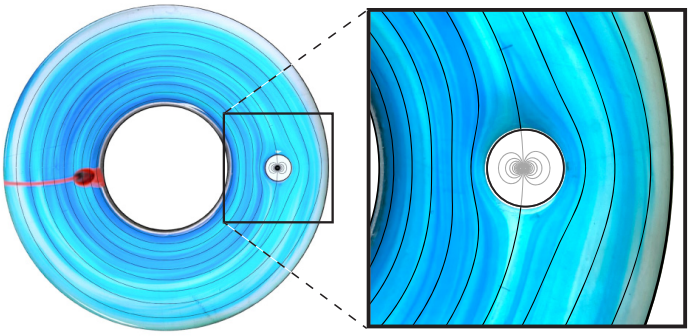


Figure 6. Dye-visualised laboratory flow (case HS) around a circular, electrically insulating obstacle (white disk). Overlain in black are approximate potential flow streamlines obtained using the Milne-Thomson circle theorem (Milne-Thomson 1938). Grey curves indicate the potential flow doublet that produces the circular obstacle streamline.

the annular device (case HS), resting on an array of permanent magnets with moderate horizontal variability in field strength (with 1 standard deviation equal to 27 % of the mean). Despite these gradients in B_z and the presence of non-negligible surface tension effects ($Bo = 1.1$), the dye streaks coincide with approximate potential flow streamlines (black overlay) obtained using the Milne-Thomson circle theorem (Milne-Thomson 1938). Thus, we expect magneto-Stokes micromixers to be robust to surface tension effects and moderate variations in magnetic field strength.

5.2. *Enhanced mixing in annular magneto-Stokes flow*

Although annular magneto-Stokes flows are vorticity free in the shallow limit, they make for robust, easily fabricated micromixing systems. Further, they exhibit multiple regimes of enhanced mixing, which we characterise here. Mixing effects in annular magneto-Stokes flows were first studied by Gleeson & West (2002) and Gleeson *et al.* (2004). The authors focused on the deep limit ($\Gamma \to \infty$), which renders the flow two-dimensional and enabled them to derive analytical asymptotic predictions for mixing time. These scaling laws are extensively supported by 2-D DNS (Gleeson *et al.* 2004), but exhibit large errors when compared with experimental results for the shallow-layer systems most relevant to compact, lab-on-a-chip applications (West *et al.* 2003). To address this gap, we generalise the scaling laws of Gleeson *et al.* (2004) to finite Γ systems, using the analytical solution developed in § 2 and validated in § 4.

The homogenisation of solute concentration c is governed by

$$Pe\,[\partial_\tau c + (1+\mathcal{R})\omega\partial_\theta c] = \frac{\mathcal{H}^2}{\rho^2}\partial_\theta^2 c + \nabla_\perp^2 c, \tag{5.8}$$

where ω is the angular velocity field. The dominance of advection over diffusion is controlled by the Péclet number (Pe), defined via the Reynolds and Schmidt (Sc) numbers as

$$Pe = ScRe, \quad Sc = \nu/\kappa_c, \tag{5.9a,b}$$

where κ_c denotes the molecular diffusivity of the solute. So long as $Re \ll \min(Pe, 1)$, the spin-up period T_{su} is the shortest time scale, and we consider the flow to be quasi-steady such that the angular velocity in (5.8) may be computed as $\omega = \bar{v}_\theta(\rho, \zeta)/\rho$ using the stationary solution (2.16).

https://doi.org/10.1017/jfm.2024.674 Published online by Cambridge University Press

We consider a simple non-axisymmetric initial condition

$$c(\rho,\theta,\zeta,0)=c_0(\theta)=\begin{cases}0, & -\pi/2<\theta\leqslant\pi/2\\ 1, & \pi/2<\theta\leqslant 3\pi/2\end{cases}, \tag{5.10}$$

and define a mixing norm m, following Gleeson *et al.* (2004), as the normalised root mean square deviation of the concentration field from its average value, $\bar{c}$:

$$m(t/T)=\frac{\|c-\bar{c}\|}{\|c_0-\bar{c}\|},\quad \|\cdot\|^2=\frac{1}{\pi(1-\mathcal{R}^2)}\int_0^1\int_0^{2\pi}\int_{\mathcal{R}}^1(\cdot)^2\rho\,\mathrm{d}\rho\,\mathrm{d}\theta\,\mathrm{d}\zeta, \tag{5.11a,b}$$

such that $m(0)=1$. The mixing time t_M is then defined as the time it takes for m to shrink to some value $M<1$. Although other metrics exist (e.g. the eigenvalue-base approach of Cerbelli *et al.* 2009), t_M benefits from its clear physical meaning and applicability to all mixing regimes. In each of these regimes, predictions for t_M/T as a function of Pe, Γ, $\mathcal{R}$ follow from the appropriate asymptotic reduction of (5.8).

5.2.1. *Diffusion-dominated regime*

For $Pe\ll 1$, lateral diffusion occurs before advection can effectively shear the tracer concentration front. Solving (5.8), (5.10) in the absence of advection and retaining the effect of the fundamental mode yields the scaling law

$$t_M/T\sim\frac{1}{\mathcal{H}^2\lambda_{11}^2}\ln\left(\frac{2\sqrt{2}}{\pi M}\right)Pe, \tag{5.12}$$

where λ_{11} is the smallest positive root of $\mathrm{J}_1'(\lambda\mathcal{R})\mathrm{Y}_1'(\lambda)-\mathrm{Y}_1'(\lambda\mathcal{R})\mathrm{J}_1'(\lambda)=0$. We assume $\mathcal{R}\gtrsim 0.1$ in (5.12) so that we may approximate an additional numerical factor arising from the average of the first radial eigenfunction with unity. Dimensionally, $t_M\sim\lambda_{11}^{-2}\ln[2\sqrt{2}/(\pi M)]r_o^2/\kappa_c$ and the mixing time is independent of depth h, as the problem is essentially two-dimensional.

5.2.2. *Taylor dispersion regime*

Depth is important at intermediate values of Pe, where vertical and radial shear enables rapid transverse diffusion in narrow channels. A centre-manifold reduction (Mercer & Roberts 1994; Roberts 1996; Ding & McLaughlin 2022; Ding 2024) of (5.8) yields the scaling law

$$t_M/T\sim\frac{(1+\mathcal{R})^2}{4\,\mathcal{C}_D}\ln\left(\frac{2\sqrt{2}}{\pi M}\right)Pe^{-1}. \tag{5.13}$$

See Appendix B for the details of this derivation. This inverse Péclet number dependence, typical of Taylor dispersion (Taylor 1953), results from an effective diffusivity $\kappa_e=\mathcal{C}_D(Pe/\mathcal{H})^2\kappa_c$ that actually increases with the vigour of advection (Pe). The dispersion coefficient $\mathcal{C}_D$ is given by

$$\mathcal{C}_D=-\frac{(1+\mathcal{R})^2}{2}\langle(\omega-\langle\omega\rangle)a_1\rangle,\quad \langle\cdot\rangle=\frac{2}{1-\mathcal{R}^2}\int_0^1\int_{\mathcal{R}}^1(\cdot)\rho\,\mathrm{d}\rho\,\mathrm{d}\zeta, \tag{5.14a,b}$$

where the function $a_1(\rho,\zeta)$ is found by solving

$$\nabla_\perp^2 a_1=\frac{(1+\mathcal{R})^2}{2}(\omega-\langle\omega\rangle), \tag{5.15}$$

subject to no-flux boundary conditions.

https://doi.org/10.1017/jfm.2024.674 Published online by Cambridge University Press

The transition between diffusion-dominated and Taylor dispersion regimes marks the onset of mixing enhancement, which occurs near the Péclet number Pe_0 at which scalings (5.12) and (5.13) are equal:

$$Pe_0 \sim \frac{\lambda_{11}\mathcal{H}(1+\mathcal{R})}{2\sqrt{\mathcal{C}_D}}. \tag{5.16}$$

5.2.3. *Advection-dominated regime*

At much higher values of Pe, advection occurs rapidly enough to shear the tracer concentration front into radially and vertically interleaved lamellae. Accordingly, we transform (5.8) into the Lagrangian frame following the flow. For $Pe \gg 1$, we recover the advection-dominated scaling

$$\tau_M \sim F^{-1}\left(\frac{\pi M}{2\sqrt{2}}\right) Pe^{1/3}, \tag{5.17}$$

which contains the one third dependence on Péclet number found in vortex flows (Rhines & Young 1983; Flohr & Vassilicos 1997). The function

$$F(x) = \left\| e^{-\frac{1}{3}(1+\mathcal{R})^2(\boldsymbol{\nabla}_\perp\omega\cdot\boldsymbol{\nabla}_\perp\omega)x^3} \right\|, \quad \text{where } \boldsymbol{\nabla}_\perp(\cdot) = \left[\boldsymbol{e_r}\mathcal{H}\partial_\rho + \boldsymbol{e_z}\partial_\zeta\right](\cdot), \tag{5.18}$$

captures the effect of shear ($\boldsymbol{\nabla}_\perp\omega$) on advection-dominated mixing. (For details of the derivation, see Appendix B.)

A Mathematica notebook, available at https://github.com/cysdavid/magnetoStokes, implements all three scaling laws (5.12), (5.13), (5.17) as a tool for practitioners, inverting (5.18) numerically and solving (5.15) with finite elements.

5.2.4. *Comparison with 3-D DNS*

We compare the asymptotic scaling predictions above with 3-D DNS of (5.8), (5.10) over five orders of magnitude in Pe. Three surveys in shallow, transitional and deep magneto-Stokes regimes ($\Gamma = 0.12, 0.85, 6$) are explored for a channel with $\mathcal{R} = 0.9$; an additional survey with $\mathcal{R} = 0.5$ and $\Gamma = 0.12$ is included for comparison. All four surveys are indicated with open markers on the regime map in figure 3(*a*) (colour scheme is maintained between figures 3, 7, 8), and the three $\mathcal{R} = 0.9$ flow profiles are plotted in figure 3(*b*,*c*). The details of the numerical method are included in Appendix C.

Figure 7 plots the dimensionless mixing times t_M/T corresponding to $M = 0.5, 0.3, 0.15$ against Pe for each DNS survey (points). The asymptotic scaling laws (5.12), (5.13), (5.17) are plotted as solid lines for each value of M (both the exponent and coefficient are predicted for these curves). The data in all four surveys follow diffusive and advection-dominated scalings. Taylor dispersion following (5.13) only appears in the shallow ($\Gamma = 0.12$) and transitional ($\Gamma = 0.85$) surveys in the narrow channel ($\mathcal{R} = 0.9$) (figure 7*a*,*b*). In the shallow ($\Gamma = 0.12$) survey, we find a fourth regime characterised by weak dispersion located between Pe^{-1} and $Pe^{1/3}$ regimes, that was not observed by Gleeson *et al.* (2004) in $\Gamma \to \infty$ flows. For the deeper and wider channels (figure 7*c*,*d*), behaviour at intermediate Pe is more complex (in the $\mathcal{R} = 0.5$ survey, Taylor dispersion disappears entirely), and we do not plot (5.13) for these surveys. Nonetheless, the transition from diffusive mixing to intermediate-Pe behaviour is accurately predicted by Pe_0 (5.16) in all four surveys (vertical dashed lines in figure 7).

https://doi.org/10.1017/jfm.2024.674 Published online by Cambridge University Press

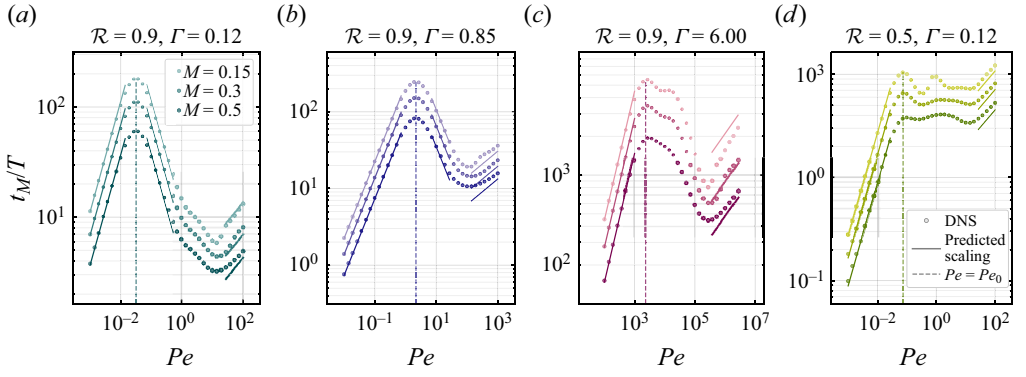


Figure 7. Mixing time t_M vs Péclet number Pe for four DNS surveys in different channel geometries ($\mathcal{R}$, Γ). Results for mixing levels $M = 0.5, 0.3, 0.15$ are indicated with darker to lighter tones. For each M, solid lines in the corresponding shade indicate predicted scaling exponents and coefficients using (5.12), (5.13), (5.17). The Taylor dispersion prediction (5.13) is omitted in panels (*c*,*d*), although the predicted onset of mixing enhancement Pe_0 (5.16) is plotted as a vertical dashed line for all four surveys.

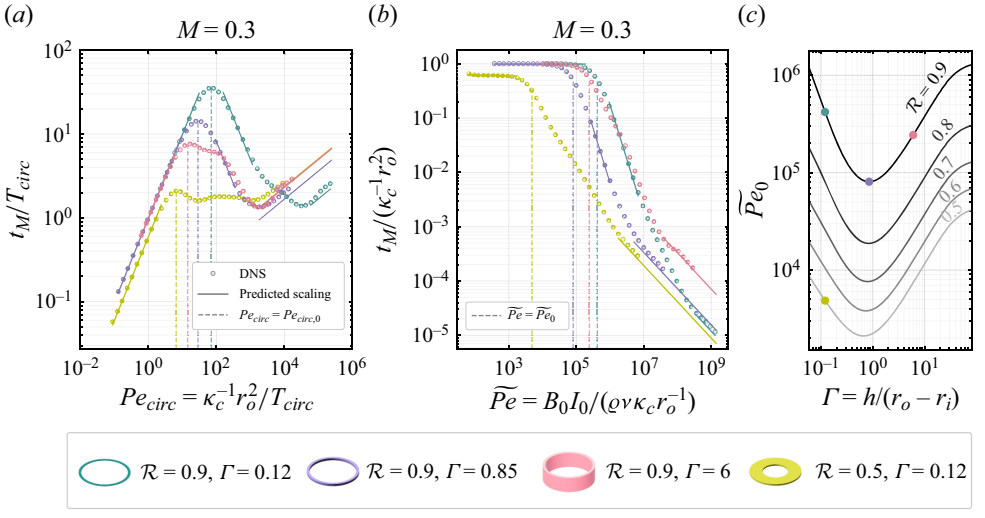


Figure 8. (*a*) The DNS results and asymptotic predictions for all four surveys rescaled using T_{circ} to show the effects of flow morphology (rather than flow magnitude) on mixing enhancement. Predicted scalings are extrapolated to the highest value of Pe_{circ} investigated. (*b*) Mixing enhancement from a practical standpoint. The data and predictions in the previous panel are rescaled such that the fluid properties and channel radius r_o may be regarded as fixed while the electromagnetic forcing $B_0 I_0$ is varied. Predicted scalings are extrapolated to the highest value of $\widetilde{Pe}$ investigated. (*c*) Asymptotic predictions for the onset of mixing enhancement $\widetilde{Pe}_0$ (using (5.16), (5.21)) as a function of depth-to-gap-width ratio Γ at different values of $\mathcal{R}$ (contour labels). Coloured points correspond to vertical dashed lines in the previous panel.

All four surveys are compared in figure 8 (for $M = 0.3$) to elucidate the effects of channel geometry ($\mathcal{R}$, Γ) on enhanced mixing. In figure 8(*a*), mixing times are scaled by the surface mid-gap circulation time,

$$T_{circ} = \pi(r_i + r_o)/u_{\theta,mid\text{-}gap}, \tag{5.19}$$

https://doi.org/10.1017/jfm.2024.674 Published online by Cambridge University Press

and the Péclet number is rescaled as

$$Pe_{circ} = \frac{u_{\theta,mid\text{-}gap} r_o^2}{U\pi h^2} Pe = \frac{r_o^2/\kappa_c}{T_{circ}}. \tag{5.20}$$

This rescaling is equivalent to considering the circulation time and outer radius to be equal for all surveys, and allowing only the height, inner radius and diffusivity to vary; this isolates the effect of the flow's morphology (e.g. the size of boundary layers) from its magnitude.

Focusing on the $\mathcal{R} = 0.9$ surveys (pink, purple and teal points), we observe two trends in figure 8(*a*) as depth-to-gap-width ratio Γ is decreased: (i) the onset of mixing enhancement is delayed ($Pe_{circ,0}$ increases; the dashed teal line lies to the right of the dashed pink line), and (ii) mixing efficiency in the advection-dominated regime increases (t_M/T_{circ} decreases; the solid teal line lies below the solid pink line on the right side of 8*a*). The onset of mixing enhancement Pe_0 is controlled by Taylor dispersion, which depends strongly on shear in the radial direction. Thus, as Γ is decreased, the sidewall boundary layers shrink (2.23*a*,*b*), Taylor dispersion is reduced and diffusion-dominated mixing persists to higher Pe. Mixing in the advection-dominated regime occurs via diffusion across lamellar structures in the tracer concentration field, which become vertically interleaved in flows dominated by vertical shear (large basal boundary layers). As Γ is decreased, the basal boundary layer grows (2.28), the tracer concentration front is vertically sheared into a spiralling interface, and t_M/T_{circ} decreases. Finally, we observe that the onset of mixing enhancement occurs earlier in the wider channel $\mathcal{R} = 0.5$ (chartreuse points) than in the narrow channel with the same depth-to-gap-width ratio (pink points). The same trends in figure 8(*a*) are present for $M = 0.15$ and $M = 0.5$.

The effects of flow morphology alone would seem to advocate for the use of deeper channels, since the onset of mixing enhancement occurs sooner (holding T_{circ} constant). However, achieving flow speeds in deep channels that are comparable to those in shallow channels is difficult in practice, as stronger magnetic fields or applied currents are required to counteract the drop in current density with depth. Thus, a practical representation of our mixing results requires one to combine the influence of flow morphology on mixing (figure 8*a*) with the influence of depth-to-gap-width ratio on flow magnitude (figure 2).

To this end, figure 8(*b*) plots mixing times scaled by the diffusive time scale r_o^2/κ_c vs the Péclet number rescaled as

$$\widetilde{Pe} = \frac{2\pi(1+\mathcal{R})^2}{\mathcal{H}^3} Pe = \frac{B_0 I_0}{\varrho \nu \kappa_c / r_o}. \tag{5.21}$$

This rescaling allows us to observe the change in mixing time vs Γ, $\mathcal{R}$, and the electromagnetic forcing ($B_0 I_0$) for a chosen solution (constant ϱ, ν, κ_c) and fixed outer radius (r_o). In the advection-dominated limit, the shallowest channels still induce the fastest mixing; in the lower right portion of figure 8(*b*), the extrapolated mixing time prediction decreases by more than fivefold between the survey with $\Gamma = 0.6$, $\mathcal{R} = 0.9$ (solid pink line) and the survey with $\Gamma = 0.12$, $\mathcal{R} = 0.9$ (solid teal line). However, the enhancement of mixing is initiated with the least effort (smallest $B_0 I_0$) for the transitional flow ($\Gamma = 0.85$; purple dashed line), out of the three $\mathcal{R} = 0.9$ surveys (pink, purple and teal dashed lines).

Figure 8(*c*) plots the predicted onset value $\widetilde{Pe}_0$ as a function of Γ for different values of $\mathcal{R}$. This shows that the transitional flow (purple point) in fact lies at a minimum in $\widetilde{Pe}_0$ for $\mathcal{R} = 0.9$. These optima, located between $\Gamma = 0.66$ for $\mathcal{R} = 0.5$ and $\Gamma = 0.85$ for $\mathcal{R} = 0.9$, result from the competing effects of sidewall boundary layer size and

https://doi.org/10.1017/jfm.2024.674 Published online by Cambridge University Press

flow speed as Γ is varied and the electromagnetic parameters are kept constant. Thus, magneto-Stokes annuli with near-unity depth-to-gap-width ratios enhance mixing for the least electromagnetic forcing.

Specific mixing applications include DNA hybridisation assays (e.g. Heule & Manz 2004), which are hindered by the extremely low chemical diffusivities typical of macromolecules in aqueous solutions (Gregory *et al.* 2016). For example, it takes more than 5 days (r_o^2/κ_c) for 20-bp DNA fragments ($\kappa_c = 5.7 \times 10^{-11}$ m^2 s^{-1}; Lukacs *et al.* 2000) to diffuse through a microfabricated annulus with $r_o = 5$ mm, $r_i = 4$ mm and $h = 425$ μm (cf. West *et al.* 2003). In contrast, applying a modest electromagnetic forcing ($I_0 = 0.1$ A, $B_0 = 25$ mT) to this system results in advection-dominated mixing ($\widetilde{Pe} = 2.2 \times 10^8$) with predicted mixing time $t_{M=0.3} = 14$ s.

Actual mixing times may be further reduced by the effects of surface tension. Deflection of the free surface at inner and outer menisci may locally reduce current density, thus enlarging the sidewall boundary layers and augmenting Taylor dispersion. Although potentially useful, these complications may be avoided by placing a no-slip upper boundary at $z = 2h$. If the total current is doubled ($I = 2I_0$), then the equations for momentum (2.10) and advection–diffusion (5.8), (5.10) are unchanged, and their solutions are simply extensions of the free-surface solutions mirrored across the $z = h$ plane. Thus, the asymptotic mixing time predictions (5.12), (5.13), (5.17) for the free-surface system also apply to a closed system with half-height h and half-current I_0.

6. Discussion

In this study, we provide the first fully analytical solution for a fundamental MHD flow: magneto-Stokes flow in a cylindrical annulus. Three flow regimes (shallow-layer, transitional and deep-layer) are distinguished based on a single geometric parameter: the depth-to-gap-width ratio Γ.

We characterise the effect of Γ on the homogenisation of a diffusing tracer, relevant to the design of microscale mixing devices (West *et al.* 2003; Gleeson *et al.* 2004). Mixing in infinitesimally thin layers ($\Gamma \to 0$) proceeds without the benefit of axial vorticity. In fact, we show that the shallow-layer asymptotic solution belongs to a class of MHD potential flows. These findings have already generated interest in analytical solutions for magneto-Stokes flow in other multiply connected channels of vanishing depth (McKee 2024).

In finite-depth channels, mixing efficiency depends strongly on the value of Γ. Using asymptotic reductions of the advection–diffusion equation validated with 3-D DNS, we show that $\Gamma \approx 1$ annuli are optimal for initiating mixing enhancement with the least electromagnetic effort ($B_0 I_0$). If the magnitude of $B_0 I_0$ is not a constraint, then the shortest mixing times may be achieved via strongly forced, advection-dominated mixing in shallow channels ($\Gamma \ll 1$).

The extensive characterisation of both momentum and tracer evolution provided here makes the annular magneto-Stokes system an excellent MHD reference flow. Among other applications, its promise as a calibration tool for particle-tracking velocimetry (e.g. Valenzuela-Delgado *et al.* 2018*a*) and particle image velocimetry draws on the simplicity of the device and robustness of the analytical solution.

Supplementary data. A supplementary Python package and accompanying Jupyter notebook that implement our theoretical predictions are available at https://github.com/cysdavid/magnetoStokes.

Acknowledgements. The authors thank E. Gomis and A. Chlarson for their early laboratory work on the magneto-Stokes annulus. C.S.D. thanks E. Zhao for her expertise in image-processing methods, which greatly

https://doi.org/10.1017/jfm.2024.674 Published online by Cambridge University Press

improved the phase-boundary-tracking code used in this study. The authors are grateful to L. Ding for his advice on the centre-manifold approach to modelling Taylor dispersion.

Funding. This research was supported by the National Science Foundation (EAR 1620649, EAR 1853196).

Declaration of interests. The authors report no conflict of interest.

Data availability statement. The laboratory and DNS data that support our findings are openly available at https://doi.org/10.5281/zenodo.12362602. Additionally, our dye-tracking velocimetry program and DNS codes may be freely accessed at https://github.com/cysdavid/magnetoStokes. A Mathematica notebook that reproduces our analytical solution is also included in this Github repository.

Author ORCIDs.
Cy S. David https://orcid.org/0009-0006-9774-1471;
Eric W. Hester https://orcid.org/0000-0003-1651-9141;
Yufan Xu https://orcid.org/0000-0001-9123-124X;
Jonathan M. Aurnou https://orcid.org/0000-0002-8642-2962.

Author contributions. C.S.D. developed the model, found the solution presented here and derived the asymptotic predictions for mixing time. E.W.H. wrote the DNS codes for both the axisymmetric 2-D standard cases and the 3-D mixing cases; C.S.D. ran these codes. C.S.D. and Y.X. carried out laboratory experiments, with Y.X. providing key insights into flow visualisation. J.M.A. conceived the idea for this study and guided its development. C.S.D. prepared all drafts of this manuscript, and all authors contributed to the final version.

Appendix A. Full axisymmetric equations and solution

The 3-D axisymmetric equations under the non-dimensionalisation in §2.1 are

$$Re\left\{\partial_\tau \upsilon_\rho + (\mathcal{R}+1)\left[\frac{1}{\mathcal{H}}(\boldsymbol{v}_\perp\cdot\boldsymbol{\nabla}_\perp)\upsilon_\rho - \frac{\upsilon_\theta^2}{\rho} + \partial_\rho \Pi\right]\right\} = \nabla_\perp^2\upsilon_\rho - \mathcal{H}^2\frac{\upsilon_\rho}{\rho^2}, \tag{A1a}$$

$$Re\left\{\partial_\tau \upsilon_\theta + (\mathcal{R}+1)\left[\frac{1}{\mathcal{H}}(\boldsymbol{v}_\perp\cdot\boldsymbol{\nabla}_\perp)\upsilon_\theta + \frac{\upsilon_\rho\upsilon_\theta}{\rho}\right]\right\} = \nabla_\perp^2\upsilon_\theta - \mathcal{H}^2\frac{\upsilon_\theta}{\rho^2} + \frac{\mathcal{R}+1}{\rho}\Upsilon(\tau), \tag{A1b}$$

$$Re\left\{\partial_\tau \upsilon_\zeta + (\mathcal{R}+1)\left[\frac{1}{\mathcal{H}}(\boldsymbol{v}_\perp\cdot\boldsymbol{\nabla}_\perp)\upsilon_\zeta + \frac{1}{\mathcal{H}^2}\partial_\zeta \Pi\right]\right\} = \nabla_\perp^2\upsilon_\zeta, \tag{A1c}$$

$$\partial_\rho(\rho\upsilon_\rho) + \rho\partial_\zeta\upsilon_\zeta = 0, \tag{A2}$$

where we define $\boldsymbol{v}_\perp = \upsilon_\rho\boldsymbol{e_r} + \mathcal{H}\upsilon_\zeta\boldsymbol{e_z}$, $\boldsymbol{\nabla}_\perp(\cdot) = [\boldsymbol{e_r}\mathcal{H}\partial_\rho + \boldsymbol{e_z}\partial_\zeta](\cdot)$, and $\nabla_\perp^2(\cdot) = [\mathcal{H}^2\rho^{-1}\partial_\rho\rho\partial_\rho + \partial_\zeta^2](\cdot)$. For vanishing meridional flow $\boldsymbol{v}_\perp$, (A1) reduces to (2.10).

In § 2.1, we provide an expression for υ_θ found by approximating the full solution to (2.10)

$$\upsilon_\theta(\rho,\zeta,\tau) = \sum_{n=1}^{\infty}\left\{\frac{2(\mathcal{R}+1)}{k_n^2\mathcal{H}}\left[\frac{\mathcal{H}}{k_n\rho} - A_n\mathrm{I}_1\left(\frac{k_n}{\mathcal{H}}\rho\right) - B_n\mathrm{K}_1\left(\frac{k_n}{\mathcal{H}}\rho\right)\right]\right.$$
$$\left. + \sum_{m=1}^{\infty} C_{mn}\left(\frac{\mathrm{J}_1(\mu_m\rho)}{\mathrm{J}_1(\mu_m)} - \frac{\mathrm{Y}_1(\mu_m\rho)}{\mathrm{Y}_1(\mu_m)}\right)\exp\left(-\frac{\mathcal{H}^2\mu_m^2 + k_n^2}{Re}\tau\right)\right\}\sin(k_n\zeta), \tag{A3}$$

where J_1 and Y_1 are first-order Bessel functions of first and second kind and each eigenvalue μ_m is the mth smallest positive root of

$$\mathrm{Y}_1(\mu)\mathrm{J}_1(\mu\mathcal{R}) - \mathrm{J}_1(\mu)\mathrm{Y}_1(\mu\mathcal{R}) = 0. \tag{A4}$$

https://doi.org/10.1017/jfm.2024.674 Published online by Cambridge University Press

Setting $\mathcal{H}^2\mu_m^2 + k_n^2 \approx k_1^2$ in the exponential term above reduces (A3) to the approximate solution (2.15). The roots of (A4) and analytical expressions for coefficients C_{mn} are provided in a Mathematica notebook available at https://github.com/cysdavid/magnetoStokes.

Appendix B. Derivation of mixing time predictions

Derivation of both the diffusion-dominated (5.12) and advection-dominated (5.17) scaling laws is facilitated by transforming (5.8) into the Lagrangian reference frame $(\rho, \tilde{\theta}, \zeta)$ according to $\theta = \tilde{\theta} + (1+\mathcal{R})\omega(\rho,\zeta)\tau$. We assume that the mixing time scales with some power α of the Péclet number, and we let $\tau = Pe^{\alpha}\tilde{\tau}$ so that (5.8) becomes

$$\partial_{\tilde{\tau}} c = Pe^{\alpha-1}\left(\frac{\mathcal{H}^2}{\rho^2}\partial_{\tilde{\theta}}^2 + \nabla_\perp^2\right) c - Pe^{2\alpha-1}(1+\mathcal{R})\tilde{\tau}\left[\nabla_\perp^2\omega + 2(\boldsymbol{\nabla}_\perp\omega\cdot\boldsymbol{\nabla}_\perp)\right]\partial_{\tilde{\theta}} c + Pe^{3\alpha-1}(1+\mathcal{R})^2\tilde{\tau}^2\,(\boldsymbol{\nabla}_\perp\omega\cdot\boldsymbol{\nabla}_\perp\omega)\,\partial_{\tilde{\theta}}^2 c. \tag{B1}$$

In the limit $Pe \to 0$, a dominant balance exists if $\alpha = 1$. This results in the classical diffusion equation, which yields (5.12) upon solution. On the other hand, two-term dominant balance in the limit $Pe \to \infty$ requires that $\alpha = 1/3$, yielding a diffusion-like equation,

$$\partial_{\tilde{\tau}} c = (1+\mathcal{R})^2\tilde{\tau}^2\,(\boldsymbol{\nabla}_\perp\omega\cdot\boldsymbol{\nabla}_\perp\omega)\,\partial_{\tilde{\theta}}^2 c, \tag{B2}$$

whose solution,

$$c(\rho,\tilde{\theta},\zeta,\tilde{\tau}) = \bar{c} + \sum_{m=1}^{\infty} C_m\sqrt{2}\cos m\tilde{\theta}\exp\left(-\frac{1}{3}(1+\mathcal{R})^2\,(\boldsymbol{\nabla}_\perp\omega\cdot\boldsymbol{\nabla}_\perp\omega)\,m^2\tilde{\tau}^3\right), \tag{B3}$$

depends on ρ and ζ parametrically through the angular velocity ω. The advection-dominated scaling law (5.17) follows from retaining only the fundamental ($m = 1$) mode in (B3).

The Taylor dispersion scaling prediction is derived using a separate procedure. We transform (5.8) according to $\theta = \vartheta + (1+\mathcal{R})\langle\omega\rangle\tau$ into the frame (ρ, ϑ, ζ) rotating with the average angular velocity $\langle\omega\rangle$. In this frame, we assume that mixing smooths out the cross-sectional averaged tracer concentration field $\langle c\rangle$ such that

$$\langle c\rangle \gg \partial_\vartheta\langle c\rangle \gg \partial_\vartheta^2\langle c\rangle \gg \partial_\vartheta^3\langle c\rangle \gg \dots, \tag{B4}$$

as $\tau \to \infty$. Given this ordering, we may effect a centre-manifold reduction (Mercer & Roberts 1994; Roberts 1996; Ding & McLaughlin 2022) of the 3-D advection–diffusion equation by adopting an asymptotic expansion for c similar to that of Ding (2024),

$$c = \langle c\rangle + Pe\,a_1(\rho,\zeta)\frac{1}{\rho_0}\partial_\vartheta\langle c\rangle + Pe\,a_2(\rho,\zeta)\frac{1}{\rho_0^2}\partial_\vartheta^2\langle c\rangle + O(\partial_\vartheta^3\langle c\rangle), \tag{B5}$$

where $\rho_0 = (1+\mathcal{R})/2$ is the mid-gap radius. The functions a_1, a_2 vanish upon cross-sectional averaging ($\langle a_1\rangle = \langle a_2\rangle = 0$) and must satisfy the same no-flux boundary conditions as does c (such that $\langle\nabla_\perp^2 a_1\rangle = \langle\nabla_\perp^2 a_2\rangle = 0$).

https://doi.org/10.1017/jfm.2024.674 Published online by Cambridge University Press

Substituting (B5) into the transformed advection–diffusion equation yields

$$\partial_\tau\left(\langle c\rangle + Pe\,\frac{a_1}{\rho_0}\partial_\vartheta\langle c\rangle + Pe\,\frac{a_2}{\rho_0^2}\partial_\vartheta^2\langle c\rangle\right) + (1+\mathcal{R})(\omega-\langle\omega\rangle)\left(\partial_\vartheta\langle c\rangle + Pe\,\frac{a_1}{\rho_0}\partial_\vartheta^2\langle c\rangle\right)$$
$$= \frac{\partial_\vartheta\langle c\rangle}{\rho_0}\nabla_\perp^2 a_1 + \frac{\partial_\vartheta^2\langle c\rangle}{\rho_0^2}\nabla_\perp^2 a_2 + O(\partial_\vartheta^3\langle c\rangle), \tag{B6}$$

which, after cross-sectional averaging $\langle\cdot\rangle$ and neglecting $O(\partial_\vartheta^3\langle c\rangle)$ terms, leaves a 1-D diffusion equation for $\langle c\rangle(\vartheta,\tau)$,

$$\partial_\tau\langle c\rangle = \mathcal{C}_D Pe\frac{1}{\rho_0^2}\partial_\vartheta^2\langle c\rangle, \tag{B7}$$

where $\mathcal{C}_D$ depends on ω and a_1 through (5.14*a*,*b*). To determine a_1 and obtain closure, we first observe from (B7) that $\partial_\tau\langle c\rangle = O(\partial_\vartheta^2\langle c\rangle)$. Then, collecting $O(\partial_\vartheta\langle c\rangle)$ terms in (B6) yields the Poisson equation (5.15), which may be solved for a_1. Finally, the advection-dominated scaling law (5.17) follows from solving (B7) and retaining only the $m=1$ mode.

Appendix C. Numerical method for 3-D mixing DNS

The 3-D simulations of the advection–diffusion equation (5.8) were performed using the pseudospectral code Dedalus. The flow field u_θ was computed using the first $\mathcal{N}$ vertical modes of the steady analytical flow solution (2.16), truncated such that the $\mathcal{N}+1$st mode changes the value of $u_{\theta,mid\text{-}gap}$ by $<0.5\,\%$. The tracer concentration c and velocity u_θ fields were discretised using Chebyshev modes in the ρ, ζ directions and real Fourier modes in the θ direction. The azimuthally discontinuous initial condition for c (5.10) was approximated by a smooth bump function to avoid Gibbs oscillations:

$$c_0(\rho,\theta) = \begin{cases} 0, & \left(\frac{\pi}{2}+\frac{\Delta\theta}{2\rho}\right)^2 \leqslant (\theta-\pi)^2 \\ S\left(\theta-\pi;\frac{\pi}{2}-\frac{\Delta\theta}{2\rho},\frac{\Delta\theta}{\rho}\right), & \left(\frac{\pi}{2}-\frac{\Delta\theta}{2\rho}\right)^2 < (\theta-\pi)^2 < \left(\frac{\pi}{2}+\frac{\Delta\theta}{2\rho}\right)^2, \\ 1, & (\theta-\pi)^2 \leqslant \left(\frac{\pi}{2}-\frac{\Delta\theta}{2\rho}\right)^2 \end{cases} \tag{C1}$$

where S is a transition function constructed following Tu (2011),

$$S(x;w,\Delta w) = \left\{1+\exp\left[\frac{\Delta w(\Delta w+2w)\left(w^2+(\Delta w+w)^2-2x^2\right)}{\left(x^2-w^2\right)\left(x^2-(\Delta w+w)^2\right)}\right]\right\}^{-1}, \tag{C2}$$

and the ramp width $\Delta\theta$ is set to $\Delta\theta = 2\pi(12/256)$ across all cases.

For efficiency reasons, we used different timestepping schemes in cases dominated by diffusion vs those with stronger advection (see Ascher, Ruuth & Spiteri 1997). The empirically determined cutoff value Pe^* between these two groups roughly coincides with Pe_0, the predicted transition between diffusion-dominated and Taylor dispersion mixing regimes. The strongly diffusive cases ($Pe < Pe^*$) used the SBDF2 scheme (Wang & Ruuth 2008), while the remainder ($Pe \geqslant Pe^*$) used the four-stage, third-order implicit–explicit

https://doi.org/10.1017/jfm.2024.674 Published online by Cambridge University Press

Γ	$\mathcal{R}$	$\mathcal{N}$	Pe^*	$(N_\rho, N_\theta, N_\zeta)$ for $Pe \geqslant Pe^*$	$\Delta\tau$ $(Pe \geqslant Pe^*)$	$\Delta\tau$ $(Pe < Pe^*)$
0.12	0.5	3	0.1	(128, 256, 64)	0.0039	0.0033
0.12	0.9	3	0.14	(128, 256, 64)	0.0057	0.0057
0.85	0.9	6	10	(128, 256, 64)	0.02	0.02
6	0.9	46	10^4	(64, 256, 128)	0.84	0.84

Table 5. Numerical parameters used for the 3-D DNS discussed in § 5.2, including the threshold Péclet number Pe^* below which SBDF2 timestepping is used instead of RK443. Spatial resolution $(N_\rho, N_\theta, N_\zeta)$ for cases with $Pe < Pe^*$ is half that of the values shown here for each survey.

Runge–Kutta (RK443) scheme (Ascher *et al.* 1997, § 2.8) and twice the spatial resolution $(N_\rho, N_\theta, N_\zeta)$ of the diffusive cases. These values, in addition to Pe^*, $\mathcal{N}$ and the timestep $\Delta\tau$ for each survey are collected in table 5. The code used for these simulations is available online (https://github.com/cysdavid/magnetoStokes).

References

Anderson, O., Baker, W.R., Bratenahl, A., Furth, H.P. & Kunkel, W.B. 1959 Hydromagnetic capacitor. *J. Appl. Phys.* **30** (2), 188–196.

Aris, R. 1956 On the dispersion of a solute in a fluid flowing through a tube. *Proc. R. Soc. Lond.* A **235** (1200), 67–77.

Ascher, U.M., Ruuth, S.J. & Spiteri, R.J. 1997 Implicit-explicit Runge–Kutta methods for time-dependent partial differential equations. *Appl. Numer. Maths* **25** (2–3), 151–167.

Baylis, J.A. & Hunt, J.C.R. 1971 MHD flow in an annular channel; theory and experiment. *J. Fluid Mech.* **48** (3), 423–428.

Ben, Y. & Chang, H.-C. 2002 Nonlinear Smoluchowski slip velocity and micro-vortex generation. *J. Fluid Mech.* **461**, 229–238.

Bertsch, A., Heimgartner, S., Cousseau, P. & Renaud, P. 2001 Static micromixers based on large-scale industrial mixer geometry. *Lab on a Chip* **1** (1), 56–60.

Bradski, G. 2000 The OpenCV Library. *Dr. Dobb's J. Softw. Tools* **25** (11), 120–125.

Braginsky, S.I. 1959 Magnetohydrodynamics of weakly conducting fluids. *Sov. J. Exp. Theor. Phys.* **37** (5), 1417–1430.

Burns, K.J., Vasil, G.M., Oishi, J.S., Lecoanet, D. & Brown, B.P. 2020 Dedalus: a flexible framework for numerical simulations with spectral methods. *Phys. Rev. Res.* **2** (2), 023068.

Canny, J. 1986 A computational approach to edge detection. *IEEE Trans. Pattern Anal. Mach. Intell.* **PAMI-8** (6), 679–698.

Cerbelli, S., Adrover, A., Garofalo, F. & Giona, M. 2009 Spectral characterization of mixing properties of annular MHD micromixers. *Microfluid Nanofluid* **6** (6), 747–761.

Cetegen, B.M. & Mohamad, N. 1993 Experiments on liquid mixing and reaction in a vortex. *J. Fluid Mech.* **249**, 391–414.

Chang, C.-C. & Yang, R.-J. 2007 Electrokinetic mixing in microfluidic systems. *Microfluid Nanofluid* **3** (5), 501–525.

Cummings, E.B., Griffiths, S.K., Nilson, R.H. & Paul, P.H. 2000 Conditions for similitude between the fluid velocity and electric field in electroosmotic flow. *Anal. Chem.* **72** (11), 2526–2532.

Davidson, P.A. 2016 *Introduction to Magnetohydrodynamics*, 2nd edn. Cambridge University Press.

Digilov, R.M. 2007 Making a fluid rotate: circular flow of a weakly conducting fluid induced by a Lorentz body force. *Am. J. Phys.* **75** (4), 361–367.

Ding, L. 2024 Diffusion-driven flows in a non-linear stratified fluid layer. *J. Fluid Mech.* (submitted) arXiv:2311.17386.

Ding, L. & McLaughlin, R.M. 2022 Determinism and invariant measures for diffusing passive scalars advected by unsteady random shear flows. *Phys. Rev. Fluids* **7** (7), 074502.

Dukhin, S.S. 1991 Electrokinetic phenomena of the second kind and their applications. *Adv. Colloid Interface Sci.* **35**, 173–196.

Early, H.C. & Dow, W.G. 1950 Supersonic wind at low pressures produced by arc in magnetic field. *Phys. Rev.* **79** (1), 186.

https://doi.org/10.1017/jfm.2024.674 Published online by Cambridge University Press

EHRFELD, W., GOLBIG, K., HESSEL, V., LÖWE, H. & RICHTER, T. 1999 Characterization of mixing in micromixers by a test reaction: single mixing units and mixer arrays. *Ind. Engng Chem. Res.* **38** (3), 1075–1082.

FAVIER, B., GODEFERD, F.S., CAMBON, C., DELACHE, A. & BOS, W.J.T. 2011 Quasi-static magnetohydrodynamic turbulence at high Reynolds number. *J. Fluid Mech.* **681**, 434–461.

FLOHR, P. & VASSILICOS, J.C. 1997 Accelerated scalar dissipation in a vortex. *J. Fluid Mech.* **348**, 295–317.

GLEESON, J.P., ROCHE, O.M., WEST, J. & GELB, A. 2004 Modelling annular micromixers. *SIAM J. Appl. Maths* **64** (4), 1294–1310.

GLEESON, J.P. & WEST, J. 2002 Magnetohydrodynamic micromixing. In *Proceeedings of the Fifth International Conference on Modelling and Simulation of Microsystems (MSM2002), Puerto Rico*, pp. 318–321. Computational Publications.

GREENSPAN, H.P. & HOWARD, L.N. 1963 On a time-dependent motion of a rotating fluid. *J. Fluid Mech.* **17** (03), 385–404.

GREGORY, T.S., CHENG, R., TANG, G., MAO, L. & TSE, Z.T.H. 2016 The magnetohydrodynamic effect and its associated material designs for biomedical applications: a state-of-the-art review. *Adv. Funct. Mater.* **26** (22), 3942–3952.

HELE-SHAW, H.S. 1898 The flow of water. *Nature* **58** (1489), 34–36.

HESTER, E.W., VASIL, G.M. & BURNS, K.J. 2021 Improving accuracy of volume penalised fluid-solid interactions. *J. Comput. Phys.* **430**, 110043.

HEULE, M. & MANZ, A. 2004 Sequential DNA hybridisation assays by fast micromixing. *Lab on a Chip* **4** (5), 506–511.

HUNT, J.C.R. & STEWARTSON, K. 1965 Magnetohydrodynamic flow in rectangular ducts. II. *J. Fluid Mech.* **23** (03), 563–581.

ISDALE, J.D. & MORRIS, R. 1972 Physical properties of sea water solutions: density. *Desalination* **10** (4), 329–339.

ISDALE, J.D., SPENCE, C.M. & TUDHOPE, J.S. 1972 Physical properties of sea water solutions: viscosity. *Desalination* **10** (4), 319–328.

JEONG, G.S., CHUNG, S., KIM, C.-B. & LEE, S.-H. 2010 Applications of micromixing technology. *Analyst* **135** (3), 460–473.

KHAL'ZOV, I.V. & SMOLYAKOV, A.I. 2006 On the calculation of steady-state magnetohydrodynamic flows of liquid metals in circular ducts of a rectangular cross section. *Tech. Phys.* **51** (1), 26–33.

KNAEPEN, B. & MOREAU, R. 2008 Magnetohydrodynamic turbulence at low magnetic Reynolds number. *Annu. Rev. Fluid Mech.* **40** (1), 25–45.

LAMB, H. 1906 *Hydrodynamics*, 3rd edn. Cambridge University Press.

LUKACS, G.L., HAGGIE, P., SEKSEK, O., LECHARDEUR, D., FREEDMAN, N. & VERKMAN, A.S. 2000 Size-dependent DNA mobility in cytoplasm and nucleus. *J. Biol. Chem.* **275** (3), 1625–1629.

MANSUR, E.A., YE, M., WANG, Y. & DAI, Y. 2008 A state-of-the-art review of mixing in microfluidic mixers. *Chin. J. Chem. Engng* **16** (4), 503–516.

MARTINO, W., DE LA MORA, J.F., YOSHIDA, Y., SAITO, G. & WILKES, J. 2006 Surface tension measurements of highly conducting ionic liquids. *Green Chem.* **8** (4), 390–397.

MCKEE, K. 2024 Magnetohydrodynamic flow control in Hele-Shaw cells. *J. Fluid Mech.* (submitted) arXiv:2404.04840.

MERCER, G.N. & ROBERTS, A.J. 1994 A complete model of shear dispersion in pipes. *Japan J. Ind. Appl. Maths* **11** (3), 499–521.

MILNE-THOMSON, L.M. 1938 *Theoretical Hydrodynamics*, 1st edn. Macmillan.

MORESCO, P. & ALBOUSSIRE, T. 2004 Experimental study of the instability of the Hartmann layer. *J. Fluid Mech.* **504**, 167–181.

NOROUZI, M. & BIGLARI, N. 2013 An analytical solution for Dean flow in curved ducts with rectangular cross section. *Phys. Fluids* **25** (5), 053602.

ORTIZ-PÉREZ, A.S., GARCÍA-ÁNGEL, V., ACUÑA-RAMÍREZ, A., VARGAS-OSUNA, L.E., PÉREZ-BARRERA, J. & CUEVAS, S. 2017 Magnetohydrodynamic flow with slippage in an annular duct for microfluidic applications. *Microfluid Nanofluid* **21** (8), 138.

PAMME, N. 2006 Magnetism and microfluidics. *Lab on a Chip* **6** (1), 24–38.

PARK, K. 1964 Partial equivalent conductance of electrolytes in sea water. *Deep-Sea Res.* **11** (5), 729–736.

POYÉ, A., AGULLO, O., PLIHON, N., BOS, W.J.T., DESANGLES, V. & BOUSSELIN, G. 2020 Scaling laws in axisymmetric magnetohydrodynamic duct flows. *Phys. Rev. Fluids* **5** (4), 043701.

PÉREZ-BARRERA, J., ORTIZ, A. & CUEVAS, S. 2016 Analysis of an annular MHD stirrer for microfluidic applications. In *Recent Advances in Fluid Dynamics with Environmental Applications* (ed. J. Klapp,

https://doi.org/10.1017/jfm.2024.674 Published online by Cambridge University Press

L. Di G. Sigalotti, A. Medina, A. López & G. Ruiz-Chavarría), Environmental Science and Engineering, pp. 275–288. Springer.

PÉREZ-BARRERA, J., PÉREZ-ESPINOZA, J.E., ORTIZ, A., RAMOS, E. & CUEVAS, S. 2015 Instability of electrolyte flow driven by an azimuthal Lorentz force. *Magnetohydrodynamics* **51** (2), 203–214.

RHINES, P.B. & YOUNG, W.R. 1983 How rapidly is a passive scalar mixed within closed streamlines? *J. Fluid Mech.* **133**, 133–145.

ROBERTS, A.J. 1996 Low-dimensional models of thin film fluid dynamics. *Phys. Lett.* A **212** (1–2), 63–71.

STELZER, Z., CÉBRON, D., MIRALLES, S., VANTIEGHEM, S., NOIR, J., SCARFE, P. & JACKSON, A. 2015*a* Experimental and numerical study of electrically driven magnetohydrodynamic flow in a modified cylindrical annulus. I. Base flow. *Phys. Fluids* **27** (7), 077101.

STELZER, Z., MIRALLES, S., CÉBRON, D., NOIR, J., VANTIEGHEM, S. & JACKSON, A. 2015*b* Experimental and numerical study of electrically driven magnetohydrodynamic flow in a modified cylindrical annulus. II. Instabilities. *Phys. Fluids* **27** (8), 084108.

SUDARSAN, A.P. & UGAZ, V.M. 2006 Multivortex micromixing. *Proc. Natl Acad. Sci. USA* **103** (19), 7228–7233.

TAYLOR, G.I. 1923 VIII. Stability of a viscous liquid contained between two rotating cylinders. *Phil. Trans. R. Soc. Lond.* A **223** (605–615), 289–343.

TAYLOR, G.I. 1953 Dispersion of soluble matter in solvent flowing slowly through a tube. *Proc. R. Soc. Lond.* A **219** (1137), 186–203.

TAYLOR, G.I. 1967 *Film Notes for Low Reynolds-Number Flows*. National Committee for Fluid Mechanics Film.

TU, L.W. 2011 *An Introduction to Manifolds*. Springer.

VALENZUELA-DELGADO, M., FLORES-FUENTES, W., RIVAS-LÓPEZ, M., SERGIYENKO, O., Lindner, L., Hernández-Balbuena, D. & Rodríguez-Quiñonez, J. 2018*a* Electrolyte magnetohydrondyamics flow sensing in an open annular channel – a vision system for validation of the mathematical model. *Sensors* **18** (6), 1683.

VALENZUELA-DELGADO, M., ORTIZ-PÉREZ, A.S., FLORES-FUENTES, W., BRAVO-ZANOGUERA, M.E., ACUÑA-RAMÍREZ, A., OCAMPO-DÍAZ, J.D., HERNÁNDEZ-BALBUENA, D., RIVAS-LÓPEZ, M. & SERGIYENKO, O. 2018*b* Theoretical and experimental study of low conducting fluid MHD flow in an open annular channel. *Intl J. Heat Mass Transfer* **127**, 322–331.

VERMA, M.K. 2017 Anisotropy in quasi-static magnetohydrodynamic turbulence. *Rep. Prog. Phys.* **80** (8), 087001.

VERNET, M., FAUVE, S. & GISSINGER, C. 2022 Angular momentum transport by Keplerian turbulence in liquid metals. *Phys. Rev. Lett.* **129** (7), 074501.

VERNET, M., PEREIRA, M., FAUVE, S. & GISSINGER, C. 2021 Turbulence in electromagnetically driven Keplerian flows. *J. Fluid Mech.* **924**, A29.

WANG, D. & RUUTH, S.J. 2008 Variable step-size implicit-explicit linear multistep methods for time-dependent partial differential equations. *J. Comput. Math.* **26** (6), 838–855.

WEST, J., GLEESON, J.P., ALDERMAN, J., COLLINS, J.K. & BERNEY, H. 2003 Structuring laminar flows using annular magnetohydrodynamic actuation. *Sensors Actuators* **96** (1–2), 190–199.

XU, Y., HORN, S. & AURNOU, J.M. 2022 Thermoelectric precession in turbulent magnetoconvection. *J. Fluid Mech.* **930**, A8.

YI, M., QIAN, S. & BAU, H.H. 2002 A magnetohydrodynamic chaotic stirrer. *J. Fluid Mech.* **468**, 153–177.

https://doi.org/10.1017/jfm.2024.674 Published online by Cambridge University Press